Consistent picture of the horizontal circulation of the Atlantic Ocean over three decades

Verónica Caínzos[1], M. Dolores Pérez-Hernández[1], Daniel Santana-Toscano[1], Cristina Arumí-Planas[1], Alonso Hernández-Guerra[1]

[1]Unidad Océano y Clima, Instituto de Oceanografía y Cambio Global, IOCAG, Universidad de Las Palmas de Gran Canaria, ULPGC, Unidad Asociada ULPGC-CSIC, Canary Islands, Spain

Correspondence to: Verónica Caínzos (veronica.cainzos@ulpgc.es)

Abstract. The circulation in the Atlantic Ocean is marked by the complex system of pathways of the Atlantic Meridional Overturning Circulation (AMOC). These currents change meridionally due to the interaction with nearby water masses. Hydrographic data provide the opportunity to characterize these currents for the whole water column with high-resolution data over the last thirty years. Moreover, inverse methods enable the quantification of absolute zonal transports across these sections, determining the strength of each current at a certain latitude in terms of mass, heat and freshwater, as well as their transport-weighted temperature and salinity. Generally, no changes can be found among decades for each of the currents in terms of transport or their properties. In the South Atlantic, the circulation describes the subtropical gyre affected by several recirculations. There are nearly 61 Sv entering from the Southern and Indian Oceans at 45°S. The South Atlantic subtropical gyre exports northward 17.0 ± 1.2 Sv and around 1 PW via the North Brazil Current and -55 Sv southward at 45°S into the Antarctic Circumpolar Current. In the north Atlantic, most of the transport is advected northward via the western boundary currents, which reduce in strength as they take part in convection processes in the subpolar North Atlantic, reflected also in the northward progress of mass and heat transport. Deep layers carry waters southward along the western boundary, maintaining similar values of mass and heat transport until the separation into an eastern branch crossing the mid-Atlantic ridge in the south Atlantic. Abyssal waters originating in the Southern Ocean distribute along the South Atlantic mainly through its western subbasin, flowing northward up to 24.5°N, subjected to an increasing trend in their temperature with time.

List of acronyms

AABW	Antarctic Bottom Water
AC	Antilles Current
ACC	Antarctic Circumpolar Current
AMOC	Atlantic Meridional Overturning Circulation
BeC	Benguela Current System
BrC	Brazil Current

CC	Canary Current	
DEBC	Deep Eastern Boundary Current	
DSOW	Denmark Strait Overflow Waters	
DWBC	Deep Western Boundary Current	
dWGC	Deep West Greenland Current	
EGC	East Greenland Current	
ERRC	East Reykjanes Ridge Current	
FC	Florida Current	
GO-SHIP	Global Ocean Ship-Based Hydrographic Investigations Program	
GS	Gulf Stream	
IC	Irminger Current	
IES	Inverted EchoSounder	
ISOW	Iceland-Scotland Overflow Waters	
LC	Labrador Current	
MAR	Mid Atlantic Ridge	
MC	Malvinas Current	
NAC	North Atlantic Current	
NADW	North Atlantic Deep Water	
NBrC	North Brazil Current	
NCEP-NCAR	National Center for Environmental Prediction and National Center for Atmospheric Research	
NIIC	North Icelandic Irminger Current	
OSNAP	Overturning in the Subpolar North Atlantic Program	
OVIDE	Observatoire de la Variabilité Interannuelle à DEcennale	
RAPID	Rapid Climate Change-Meridional Overturning Circulation and Heatflux Array	
SEC	South Equatorial Current	
SPNA	Subpolar North Atlantic	
TW	Transport-weighted	
uWGC	Upper West Greenland Current	
WOCE	World Ocean Circulation Experiment	

35 DWBC
40 GO-SHIP
45 LC
50 NBrC
55 RAPID
60 WOCE

1 Introduction

The Atlantic Ocean is connected by its meridional overturning circulation (AMOC), which can be considered as two overturning cells that meet at deep layers. The upper cell consists of upper warm, saline waters that are transported

northward and, eventually, get colder, fresher and denser and travel southward in deep layers. This cell is balanced by the lower cell of the AMOC, in which the southward deep layers are returned northward by the abyssal layers (Caínzos et al., 2022; Kersalé et al., 2020). This proves to be a remarkable characteristic of the Atlantic Ocean, since it maintains a net northward transport of heat across all latitudes, contrasting to the southward heat transport appearing in other oceans in the subtropical gyre of the southern hemisphere (Ganachaud and Wunsch, 2003; Jayne and Marotzke, 2001; Forget and Ferreira, 2019).

The complex system of currents making up the AMOC has been often oversimplified, despite the multiple pathways connecting its different elements (Bower et al., 2019). Lagrangian studies have provided very useful insights of ocean currents, firstly on the surface and then for the full water column, mapping the spatial structure of the ocean circulation as they naturally drift (Bower et al. 2019, Davis et al., 1992). However, most of these measurements are currently limited to the top-most 2000 m since this is the maximum depth of the Argo profiles. Deep-Argo profilers could provide in the future a continuous quantification of the ocean below 2000 m (Foppert et al., 2021; Johnson et al., 2015, 2019). Moreover, data from mooring arrays at key locations have provided continuous measurements over the last years and could be useful to quantify currents at these chosen latitudes (Lozier et al., 2017; Cunningham et al., 2007; Johns et al., 2011; Kanzow et al., 2006; Hummels et al., 2015; Meinen et al., 2013; Kersalé et al., 2020). A combination of these international arrays has evolved into synthetic observational time series of the AMOC (McCarthy et al., 2020). However, with the earlier starting date of these arrays being the 2000s, the time series are sometimes too short to study variability and lack the necessary spatial resolution to fully resolve the structure or variability of currents. Therefore, ship-based observing systems are the only current alternative to study the full-water column of the ocean at periodic intervals that allow us to expand back into the 1990s.

Repeat hydrographic sections have been made available since the 1950s with the efforts of the International Geophysical Year. Near the end of the twentieth century, continuous basin-scale measurements were emphasized under the World Ocean Circulation Experiment (WOCE) and, later, the Global Ocean Ship-Based Hydrographic Investigations Program (GO-SHIP; Talley et al., 2016). Full-depth water column, high-resolution measurements of temperature and salinity enable the computation of geostrophic velocity for each hydrographic station pair relative to an assumed level of no motion. Inverse modelling provides a useful tool in computing the absolute geostrophic velocity (Wunsch, 1996). Moreover, it enables the estimation of meridional property transports from high-resolution hydrographic data, accompanied by uncertainties obtained along the inverse solutions (Ganachaud and Wunsch, 2003; Macdonald and Wunsch, 1996; Fu et al., 2020; Lumpkin and Speer, 2007).

Ganachaud and Wunsch (2000) have previously provided a globally consistent circulation scheme using WOCE sections for the global ocean using inverse modelling. Furthermore, they also described the regional aspects of that circulation (Ganachaud and Wunsch, 2003). Their suggested circulation in the Atlantic Ocean agrees with estimates from other global and regional studies spanning over the previous 30 years. Their solutions rely on the assumption that large-scale quantities are close to the time mean. The remaining uncertainties are dominated by oceanic variability in the density and other properties, which mainly originated from a lack of measurements and large seasonality.

Caínzos et al. (2022) have published updated estimations of the AMOC, heat and freshwater transports across the Atlantic Ocean using WOCE and GO-SHIP sections for the last thirty years. The solutions were obtained using inverse models, one for each of the last three decades – 1990 to 1999, 2000 to 2009 and 2010 to 2019. For that study, the authors focused on the possible changes of the AMOC at each latitude available in each model. The results show no changes in the AMOC for all sections analysed over the whole Atlantic for the last thirty years for either mass, heat or freshwater.

In this study, we will describe the horizontal circulation in each section and try to quantify the strength of surface, deep, and abyssal currents in the Atlantic Ocean as well as their changes over the last three decades. Additionally, we have also investigated the changes in heat and freshwater content and their transformation across latitudes. Throughout the text, we first describe the hydrographic data and the methodology applied to them in Section 2. We then describe the properties of the currents present for all latitudes in Section 3, dividing them into surface, deep and bottom currents. These currents are discussed in this study following the direction of their flow, from their origin to their destination, to be able to compare how they might change on their way. However, the currents in the figures are depicted from north to south.

2 Data and methods

2.1 Hydrographic data

We have compiled zonal hydrographic sections for the last three decades (1990-99, 2000-09, 2010-19) as part of WOCE and GO-SHIP programs. The selected sections span the whole Atlantic basin, from 45°S to 53°N+58°N in the first decade and from 30°S to 53°N+58°N for the last two decades (**Figure 1**). Deviations of some stations from the nominal latitude appear mostly over the western and eastern boundaries and over the platform, correcting the track line to a perpendicular angle to the main current. Only three sections appear in all three decades: 30°S, 24.5°N and the northernmost sections (at an average latitude of 55°N) divided into the western (53°N) and eastern (58°N) basins. **Table 1** summarizes the chosen sections and their characteristics, as well as the period when data were collected. Vertical sections for temperature and salinity for each cruise are available in the Supporting Information of Caínzos et al. (2022).

We have identified the main water masses in these sections and defined a reference level of no motion located at the interface between the southward flowing North Atlantic Deep Water (NADW) and the northward Antarctic Bottom Water (AABW), following Caínzos et al. (2022), Hernández-Guerra et al. (2019) and McDonagh and King (2005). This neutral density (γ^n) reference layer is used in the thermal wind equation to estimate geostrophic velocities and transports. The value of the reference layer for each section is specified in **Table 1.** If any pair of stations fail to reach this value of neutral density, then the deepest common level is used instead of the reference layer. This usually happens over the continental slope, and the velocity in the triangular section below this level is taken to be constant and equal to the velocity at the lowest common level.

The water column is divided into 11 layers defined by isolines of the same neutral density selected according to the presence of different water masses (Hernández-Guerra et al., 2019; Talley, 2008). The Ekman transport is estimated using the

130 National Center for Environmental Prediction and National Center for Atmospheric Research (NCEP–NCAR) surface winds. We compute the Ekman transport for the time of the cruise and include it in the first layer of each section. If outcropping is found at the surface, we measure the percentage of each layer at the surface and then associate these different weights to the Ekman transport for each outcropping layer.

2.2 Inverse model

135 Applying geostrophy to each pair of hydrographic stations, we obtain relative velocities referenced to a supposed level of no motion. However, in truth this reference level has a velocity different from zero. Inverse models have been widely used to determine the unknown geostrophic reference velocities for each hydrographic station pair. The most basic constraints applied to inverse models are based on the continuity equation, either in mass, heat and/or salinity content (Wunsch, 1978, 1996). The inverse model equations are represented in matrix form as:

140 $$\mathbf{Ab} + \mathbf{n} = -\mathbf{Y}, \tag{1}$$

where $\mathbf{A}$ is a M $\times$ N matrix, there N is the total number of unknowns and M is the number of transport constraints (or equations), $\mathbf{b}$ is a column vector of length N containing the unknowns of the system, and $\mathbf{n}$ is a column vector of length M that includes the noise of each constraint. $\mathbf{Y}$ is a column vector of length M with the initial transports and externally imposed mass transports.

145 The inverse model used here is the same as in Caínzos et al. (2022). For each decade, the inverse model links boxes between adjacent sections from south to north. For a single box, we have conserved mass and salinity content. Mass is conserved for the whole box for all station pairs of both sections and considers the Ekman corrections for each section. Moreover, to define the continuity of mass transport for each single layer, conservation of each layer was imposed between both sections, with Ekman correction in the outcropping layers. Regional constraints, based on direct current measurements and topographic

150 features, are applied to each section, despite having different station pairs and neutral density layers affected. In addition to mass conservation, we have also constrained the salinity content of each single section. Using salinity allows for changes in freshwater across the section while still conserving mass. The system of unknowns includes the velocities at the reference level and the adjustment of the Ekman transport in the first layer. The same model configuration is used for each model, so that differences in the model solution are attributable to changes in circulation. Further in-depth descriptions of the reference

155 level, a priori estimates and uncertainties, and sensitivity tests applied to these inverse models appear in the Supporting Information of Caínzos et al. (2022).

The Gauss-Markov estimator is applied to solve this highly underdetermined system of equations (Wunsch, 1996) with a minimum error variance solution from the initial estimates of the unknowns - the velocities at the reference level (**b**) and the adjustments to the Ekman transport (ΔT_{Ek}). To solve it, we first need a priori estimates and uncertainties that give an initial

160 approximation to the actual value. Despite obtaining similar results, this study provides smaller uncertainties than other

global inverse solutions (Ganachaud, 2003) and decadal studies (Fu et al., 2020). This was achieved by using physical constraints with a simpler model with only the velocities at the reference level and the Ekman adjustments as unknowns.

However, we have to be aware that there are some limitations associated with inverse modeling of hydrographic data, as inverse models with single-section snapshots are presumably subject to aliasing (Frajka-Williams et al., 2019; Wunsch and Heimbach, 2006). Therefore, each inverse solution could be interpreted as representative of a relatively short time interval (Fu et al., 2020) or could give information of monthly variations of the AMOC (Bryden et al., 2005b). Ganachaud (2003a) refer to their estimates as time-average transoceanic transports with realistic uncertainties, although they acknowledge the temporal sampling problem inherent to the discrete sampling of hydrographic data. Therefore, the validity of hydrographic data to reconstruct climatological estimates is an open debate.

Moreover, inverse models are able to resolve the circulation satisfactorily in most regions, except at subpolar latitudes where the barotropic component of the current is strong and the velocity at the reference level from the inverse model does not take into account this barotropic velocity (Álvarez et al., 2002). Therefore, mass transports in these regions can be underestimated. This issue could be resolved with the use of LADCP/SADCP direct velocity measurements capturing this barotropic component, but these data are not often available (Hernández-Guerra and Talley, 2016; Casanova-Masjoan et al., 2018; Lherminier et al., 2007, 2010; Holliday et al., 2018; Arumí-Planas et al., 2023). As a result, all uncertainties quoted are formal results that depend on the limited assumptions imposed on the inverse model and should not be regarded as strictly limiting the total strength of these time mean currents.

2.3 Adjusted transports

Using the results from the inverse model we can obtain the absolute velocity, considering adding the adjustments to the velocities at the reference level (**b**) to the geostrophic velocity between each pair of stations, v_r. The adjusted mass transport (T_M) can be computed integrating the absolute velocity over an area **A** defined by a certain horizontal and vertical extension:

$$T_M = \int \rho \, (v_r + b) \, dA, \tag{2}$$

where ρ is the density. Heat transport (T_H) can be computed as

$$T_H = \int c_p \, \theta \, \rho \, (v_r + b) \, dA, \tag{3}$$

where c_p is the heat capacity of sea water and θ is the potential temperature.

The freshwater flux (FW) has been estimated as the freshwater divergence, which represents the difference between the total freshwater flux and the volume flux through the Bering Strait (Caínzos et al., 2022; McDonagh et al., 2015; Bryden et al., 2011):

$$FW = -\frac{T_i^M S' - \int \rho \, S' \, (v_r + b) \, dA}{S_0}, \tag{4}$$

where T_i^M is the interbasin mass transport, i.e., across the Bering Strait (-0.8 Sv), S' is the salinity anomaly and S_0 is the area-weighted section average.

The longitudinal extension of each current has been defined based on the eastward accumulated horizontal mass transport, defining the chosen station pairs with a consistent slope in the accumulated horizontal mass transport. The vertical extension is ascribed with the net mass transport integrated over the chosen station pairs with the same flow direction. In this study, we have focused on the main currents, restricted to certain longitudinal and vertical regions. Therefore, no mass transport balance can be obtained only from these main features of the circulation. The mass balance within a transoceanic section could be obtained after accounting for the transport over the ocean interior.

3 Results and discussion

This study uses a combination of hydrographic sections taken over the course of thirty years to describe the intricate network of currents that make up the AMOC throughout the Atlantic basin. With the results from the inverse models, we can measure the main important currents that flow along the Atlantic Ocean. Here we assess their transport in terms of mass (**Figure 2**), heat (**Figure 3**), and freshwater transport (**Figure 4**).

3.1 Boundary and surface currents

3.1.1 Malvinas Current

The Malvinas Current (MC) is a cold and nutrient-enriched current originating from a northernmost branch of the northward Antarctic Circumpolar Current (ACC) known as the Subantarctic Front that enters the South Atlantic as part of the cold-fresher water route (Bower et al., 2019). It keeps flowing along the continental shelf of Argentina colliding at ~39°S with the warmer and saltier southward Brazil Current (BrC), and then both currents turn offshore (Artana et al., 2018; Legeckis and Gordon, 1982; Garzoli, 1993; Vivier and Provost, 1999a; Goni et al., 1996). The MC is observed as a northward transport of 37.2 ± 2.0 Sv at 45°S over the platform and slope of the 1990-99 inverse solutions (**Figure 2**), extending 109 km from the coast to 58.6°W (**Figure 5 l, m** and **Table 2**). The current, extending from the surface up to 1200 m, flows more intensely along the layer between 27.23 and 27.58 kg m^{-3} (~650 m), carrying 19.2 ± 1.5 Sv, representing over 50% of its total strength. The MC transports equatorward 0.54 ± 0.02 PW of heat (**Figure 3**) and 0.07 ± 0.01 Sv of freshwater (**Figure 4**), carrying waters with mean transport-weighted (TW) salinity of 34.265 and temperature of 3.66°C.

The mass transport estimation coincides with the 24-year mean transport of 37.1 ± 2.6 Sv at 41°S from in situ current velocity and satellite altimetry from Artana et al. (2018). They have also found no significant trend in the MC transport, with larger annual standard deviations mainly associated with smaller mean transports. Earlier estimations using direct velocity measurements at the same location also agree with these results, manifesting the high variability of the MC: 41.5 Sv with a standard deviation of 12 Sv for December 1993 to June 1995 (Vivier and Provost, 1999b) and 34.3 Sv for December 2001 to February 2003 (Spadone and Provost, 2009). Other estimations from inverse solutions using hydrographic data have found slightly larger results (45 ± 7 Sv by Maamaatuaiahutapu et al., 1998; 42.7 ± 6.5 Sv by McDonagh and King, 2005). Further

south, at 51ºS, the Subantarctic Front has also shown large interannual variability, carrying 32.6 Sv in 1999 while 17.9 Sv in 2010 (Pérez-Hernández et al., 2017), being the former consistent with our MC estimates.

This section is subjected to the presence of fronts designated by large-scale features of the ACC (**Figures 2, 3 and 4**; Orsi et al., 1995; Sokolov and Rintoul, 2009). The subtropical front marks the northernmost presence of subantarctic waters and can be found at 45°S (Smythe-Wright et al., 1998) extending over 463 km between 15.0°W and 10.1°W (**Figure 5 m** and **Table 2**), occupying a large part of the barotropic water column (up to ~3000 m deep). Across this front, there is a net southward mass transport of -55.5 ± 5.6 Sv, effectively removing -1.09 ± 0.07 PW of heat and -0.14 ± 0.03 Sv of freshwater out of the South Atlantic.

3.1.2 Brazil Current

The westward South Equatorial Current bifurcates when it reaches the continental shelf off Cape São Roque (**Figure 1**), dividing into the northward flowing North Brazil Current (NBrC) and the southward western boundary Brazil Current (BrC), carrying warm subtropical water (Stramma et al., 1990).

At 19°S (**Figure 5 c, d** and **Table 2**), the BrC transports southward -19.7 ± 1.3 Sv of water (**Figure 2**) in an approximate barotropic pattern up to 27.84 kg m^{-3}, spanning down to roughly 1500 m depth, and extending 37 km from the coast to 37.1°W. The heat transport carried out by this current is -0.79 ± 0.05 PW (**Figure 3**), while maintaining a northward flux of 0.06 ± 0.03 Sv of freshwater (**Figure 4**) for the 1990-99 solutions. The BrC at this latitude is followed up by a narrow recirculation between 36.7°W and 36.4°W over a similar depth range, transporting northward 19.3 ± 2.1 Sv of mass transport, 0.67 ± 0.08 PW of heat transport and 0.06 ± 0.04 Sv of freshwater flux.

The BrC at 24°S (**Figure 5 f, g** and **Table 2**) is manifested as a narrow current with a recirculation of almost the same magnitude, followed by another southward flowing current occupying a larger horizontal extension toward the ocean interior. The BrC occupies a longitudinal extent of 25 km from the coast to 40.8°W in 2000-09 and 47 km from the coast to 40.6°W in 2010-19. The vertical extension of the BrC at 24°S is reduced, reaching the γ^n interface of 27.00 kg m^{-3} (depth of ~500 m). The transports decrease compared to 19ºS for mass (-4.7 ± 0.4 and -12.0 ± 0.7 Sv; **Figure 2**) and heat (-0.39 ± 0.02 and -0.88 ± 0.04 PW; **Figure 3**), with no significant changes in the northward flux of freshwater (0.04 ± 0.01 and 0.16 ± 0.01 Sv; **Figure 4**) for both the solutions of models including data from 2000-09 and 2010-19, respectively. These southward transports of mass are consistent with the results of -9.6 Sv, -8.6 Sv and -7.3 ± 0.9 Sv from Stramma, (1989), Garzoli et al. (2013) and Arumí-Planas et al. (2023), respectively, although a previous inverse solution at this latitude has found slightly lower values (-5.8 ± 0.1 Sv, Evans et al. 2017). At this latitude appears a recirculation 136 and 43 km eastward of the BrC, reaching depths of ~700 m. This current recirculates a large part of the BrC transport, with 8.9 ± 1.4 and 10.5 ± 0.9 Sv of northward mass transport for each decade, 0.57 ± 0.09 and 0.70 ± 0.05 PW of heat transport and southward freshwater fluxes (-0.03 ± 0.03 and -0.07 ± 0.02 Sv).

The Brazil Current at 30°S gets broader, extending 443 km from the coast to 42.9°W, from 282 km from 46.3°W to 43.6°W and 122 km from the coast to 46.5°W in each decade. Moreover, the BrC deepens its lower interface (27.23 kg m^{-3}), reaching

slightly larger depths for the inverse solutions containing sections from 1990-99 and 2000-09, and a similar depth for those within 2010-19 (678, 735 and 505 m). The BrC at this latitude presents similar structures for the first two decades (**Figure 5 i, j** and **Table 2**), with a decreasing southward transport among each cruise and a sharp decrease for the last one (-26.7 ± 1.6, -22.2 ± 1.5 and -9.5 ± 0.7 Sv for the 1990-99, 2000-09 and 2010-19 solutions, respectively; **Figure 2**). Similar tendencies appear for both heat transport (-1.63 ± 0.09, -1.31 ± 0.08 and -0.64 ± 0.04 PW; **Figure 3**) and freshwater flux (0.16 ± 0.02, 0.09 ± 0.02 and 0.05 ± 0.01 Sv; **Figure 4**). At this latitude, the strengthening of the BrC is counteracted by a recirculation occurring eastward of the BrC, redirecting northward over half of the current (16.4 ± 1.9, 15.9 ± 2.0 and 13.2 ± 1.4 Sv of mass transport, 0.85 ± 0.07, 0.80 ± 0.08 and 0.76 ± 0.07 PW of heat transport and -0.16 ± 0.03, -0.14 ± 0.03 and -0.06 ± 0.02 Sv of freshwater). The combination of BrC and its recirculation increased from 24°S to this latitude, agreeing with the estimations of Peterson and Stramma (1991) that indicate an intensification of 5% per 100 km south of 24°S. This southward intensification has been corroborated with results from hydrography (Stramma, 1989; Garzoli et al., 2013) and a combination of Argo floats and satellite altimetry (Schmid and Majumder, 2018). At a latitude close to 27°S, the northern branch of the intermediate circulation moves westward from the eastern boundary until it encounters the South American continental margin. At this point, the intermediate flow breaks into two branches, one veering equatorward and flowing against the BrC north of 27°S, which may result in the reduced BrC at 24°S, and the other feeding the BrC with a stronger net southward transport in intermediate layers at 30°S (Legeais et al., 2013; Boebel et al., 1999; Valla et al., 2018).

The BrC at 19°S presents TW temperatures of 10.21°C and salinities of 35.113, which increases on its way southward to 24°S (21.03 and 18.64°C for the 2000-09 and 2010-19 decades and 36.340 and 36.066). The values for the recirculation at 24°S are slightly reduced compared with BrC (16.17 and 16.69°C and 35.617 and 35.785). Properties at 30°S appear to decrease among the first decades for both TW temperature (15.47 and 14.96°C) and TW salinity (35.611 and 35.558), with an increase for the last decade on both TW temperature and salinity (16.99°C and 35.900, respectively). The recirculation at 30°S presents values lower than those of the BrC at the same latitude (TW temperatures of 13.09, 12.75 and 14.54°C and TW salinities of 35.300, 35.248 and 35.271).

3.1.3 Benguela Current System

The northward Benguela Current System (BeC) is the relatively strong eastern boundary current of the South Atlantic subtropical gyre, with a varying longitudinal extension (Wedepohl et al., 2000). The BeC can be first identified at cape Agulhas (located at 34.8°S, 20.0°E) for the 45°S section (**Figure 5 m, n** and **Table 2**), extending from 2.9°E to the coast over 1335 km in the horizontal and 650 m in the vertical, up to a γ^n of 27.23 kg m^{-3}. The BeC reaches the southern tip of the African continent transporting 24.0 ± 2.3 Sv of mass, 1.19 ± 0.11 PW of heat and -0.07 ± 0.02 Sv of freshwater (**Figures 2, 3 and 4**). At this latitude, the BeC carries water with TW temperatures of 12.53°C and TW salinities of 35.057.

The BeC at 30°S (**Figure 5 j, k** and **Table 2**) occupies narrower extensions (~310 km) from ~11.5°E to the coast, influencing the first 500 m of the water column, maintaining the same γ^n lower interface of 27.23 kg m^{-3}. The BeC carries similar mass transports of 12.1 ± 1.2, 12.1 ± 1.2, and 13.5 ± 1.0 Sv for all three cruises included in the solutions for the 1990-

99, 2000-09 and 2010-19 decades, respectively, accompanied by 0.60 ± 0.05, 0.61 ± 0.06 and 0.67 ± 0.05 PW of heat transport. The freshwater flux carried southward by the BeC appears to increase for the last decade (-0.02 ± 0.01, -0.02 ± 0.01 and -0.05 ± 0.01 Sv). Garzoli et al. (1996) studied the time evolution of the BeC at 30°S and found large variability for the transport and velocity records due to the passage of Agulhas rings, with a mean transport of 16 Sv, comparable to our estimations.

At 24°S the BeC extends over ~90 km, from ~8.9°E to the coast (**Figure 5 g, h** and **Table 2**), maintaining similar vertical structures from the surface up to ~550 m deep for γ^n of 27.23 kg m^{-3}. However, different transports appear (8.7 ±1.3 and 4.6 ± 0.8 Sv for mass; 0.44 ± 0.06 and 0.25 ± 0.04 PW for heat), significantly weaker than those at 30°S.

Our results from 30°S and 24°S manifest the strong variability of the Benguela Current, with no clear pattern (**Figures 2, 3 and 4**). At 19°S, the BeC presents the same narrow extension as in 24°S (113 km) from 8.1°E to the coast, whilst reaching in the vertical from the surface up to 500 m (**Figure 5 d, e** and **Table 2**). There is a slight reduction at 19°S, reaching values of 2.3 ± 1.2 Sv for mass transport, 0.13 ± 0.05 PW of heat transport and null freshwater flux, with no continuity north of 19°S.

The BeC is fed by subtropical thermocline waters from the Indian and South Atlantic Oceans, as well as saline, low-oxygen tropical Atlantic water and cooler, fresher subantarctic water (Garzoli and Gordon, 1996; Garzoli et al., 1996). Model studies have found that around most of the transport entering the South Atlantic via the Agulhas leakage carries waters from the Indonesian Throughflow and the south of Australia (Durgadoo et al., 2017). Thus, the BeC at 30°S advects waters with TW temperatures of 12.66, 12.75 and 12.66°C and TW salinities of 34.998, 35.071 and 35.102 for each decade, respectively. Similar values are maintained for the 24°S sections, with TW temperatures of 12.69 and 13.94°C and TW salinities of 35.019 and 35.096 for the last two decades. Both TW temperature and salinity increase for waters of the BeC reaching 19°S (14.06°C and 35.262, respectively).

3.1.4 South Equatorial Current

The South Equatorial Current (SEC) is a broad current flowing westward toward the Brazilian shelf, where it bifurcates at Cape São Roque (**Figure 1**), with one branch heading north as the North Brazil Current (NBrC) and the other, weaker, southward as the BrC.

The SEC at 30°S occupies the first ~700 m of the water column, at depths above 27.23 kg m^{-3}, occupying large extensions of ~2700 km between 18.4°W and 8.5°E for the cruise included in the 1990-99 solution, 19.0°W and 7.6°E for the cruise in 2000-09 and 19.8°W and 9.0°E for the recent cruise included in the solution for 2010-19 (**Figure 5 j** and **Table 2**). The SEC net northward transports of mass (16.9 ± 1.9, 14.6 ± 2.1 and 15.9 ± 1.9 Sv; **Figure 2**) and heat (0.86 ± 0.09, 0.76 ± 0.10 and 0.80 ± 0.09 PW; **Figure 3**) show similar values among realizations, with null values for the freshwater flux.

At 24°S the SEC has become slightly shallower, with depths of ~625 m for the 27.23 kg m^{-3} γ^n interface. However, on its way northwestward, it has expanded horizontally, occupying now longitudinal extensions of ~3300 km between 24.2°W and 7.4°E for the cruise within 2000-09 and 26.1°W and 7.6°E for the one within 2010-19 (**Figure 5 g** and **Table 2**). The transports associated to the SEC are similar to those at 30°S, with stable values of 16.5 ± 1.7 and 16.5 ± 1.6 Sv for mass

transport, 1.00 ± 0.10 and 1.04 ± 0.10 PW for heat transport (**Figures 2 and 3**). The values at 19°S show a SEC reaching depths of ~515 m for the same 27.23 kg m^{-3} lower interface, while maintaining a similar horizontal extent (~3200 km) over longitudes 23.2°W and 7.0°E (**Figure 5 d** and **Table 2**). The mass transport at this latitude has decreased significantly (9.0 ± 1.9 Sv), accompanied by a reduction in heat transport (0.60 ± 0.11 PW).

325 The salinities present in the South Atlantic are subject to the intense surface evaporation in the region between 8°S and 25°S. The SEC starts carrying waters at 30°S with TW temperatures of 12.85, 13.22 and 12.70°C and TW salinities of 35.060, 35.142 and 35.179. Those properties increase on its way northwestward, reaching at 24°S TW temperatures of 15.35 and 15.94°C and TW salinities of 35.451 and 35.537 for the last two decades. At 19°S, the SEC carries waters with TW temperature of 16.90°C and TW salinity of 35.644.

330 ### 3.1.5 North Brazil Current

The northward North Brazil Current (NBrC) carries warm water from the south Atlantic along the coast of Brazil, across the equator, and into the northern hemisphere, acting as a conduit for cross-equatorial transport of upper ocean waters as part of the AMOC. This northward branch of the SEC can be found at 11°S (**Figure 5 a, b** and **Table 2**), sampled in the 1990-99 decade, extending from the coast to 34.7°W over 130 km. Its vertical structure presents two maximums in the circulation,

335 with a surface layer from the surface to 26.14 kg m^{-3} (~203 m) and a subsurface layer from 26.45 to 27.00 kg m^{-3} (~400 to ~500 m), carrying 5.0 ± 0.4 and 5.7 ± 0.3 Sv, respectively. The total equatorward transport is 17.0 ± 1.2 Sv of mass and 0.98 ± 0.05 PW of heat, associated with a southward freshwater flux of -0.19 ± 0.03 Sv (**Figures 2, 3 and 4**). The strong current estimated agrees with the 15-month mean value of 16 ± 2 Sv obtained by Garzoli et al. (2004) from Inverted EchoSounders (IES) and are slightly lower than the Argo-based solutions of Tuchen et al. (2022) of 21.8 Sv. The NBrC presents higher TW

340 temperatures (14.59°C) and salinities (35.509) than the ones found at 19°S for the BrC.

3.1.6 Florida Current

The Florida Current (FC) stretches over ~70 km from the Florida Straits up to Cape Hatteras (**Figure 1**), sourcing mainly from the Loop Current coming from the Gulf of Mexico (Maul and Vukovich, 1993) and, to a lesser extent, from the Antilles Current (AC), transporting warm waters northward (**Figure 6 h** and **Table 2**) in a water column of ~600 m deep. The FC

345 shows different values of mass transport across time (34.5 ± 0.3, 32.1 ± 0.3 and 31.3 ± 0.3 Sv for the cruises within 1990-99, 2000-09 and 2010-19 decades, respectively; **Figure 2**), also manifested in its heat transport (2.70 ± 0.02, 2.43 ± 0.02 and 2.31 ± 0.02 PW; **Figure 3**), combined with their TW temperature (19.84, 19.16 and 18.65°C). The freshwater flux associated to the FC, although not as important as the heat transport, also presents relatively high southward values (-0.17 ± 0.01, -0.09 ± 0.01 and -0.14 ± 0.01 Sv; **Figure 4**), associated with quite stable values of TW salinity (36.120, 36.201 and 36.098), with

350 differences of less than 0.1.

Our results can be compared with the nearly continuous monitoring of the FC transport since 1982 at 27°N from submarine cable measurements, which yields an average transport of 31.8 ± 0.1 Sv (Piecuch, 2020), with decadal values of 32.5 ± 1.2

Sv for 1990-99, 32.4 ± 1.0 Sv for 2000-09 and 31.9 ± 0.6 Sv for 2010-19 for the 95% percentile. These results agree with the FC transports estimated from the inverse models although the value for the cruise carried out during 1990-99 is slightly

355 larger. Its mean seasonal cycle has a 3.3-Sv annual periodicity, with maxima in mid-July and minima in mid-January (Atkinson et al., 2010), linking its variability to the North Atlantic Oscillation (Baringer and Larsen, 2001) coupled with a long-term weakening (Piecuch, 2020).

3.1.7 Antilles Current

In the western coast of the subtropical North Atlantic, the Antilles Current (AC) flows northward and then northwestward

360 around the Bahamas Islands (**Figure 1**) before joining the FC and Gulf Stream (GS). The AC at 24°N occupies the first ~700 m of the water column, from the surface to 27.23 kg m^{-3}, but presents different longitudinal extensions among cruises (125 km from Cape Hatteras to 74.3°W in 1990-99, and ~38 km from Cape Hatteras to 76.4°W and 76.7°W in 2000-09 and 2010-19, respectively).

The values of mass transport for the AC show similar values for the first two cruises and a sharp decrease for the most recent

365 estimation (12.8 ± 1.0, 13.2 ± 0.4 and 7.5 ± 0.3 Sv), with a similar pattern for its heat transport (0.98 ± 0.07, 0.97 ± 0.03 and 0.56 ± 0.02 PW) as shown in **Figure 6 g, h** and **Table 2**. The decreasing values in heat transport can be attributed to a combination of a reduction in mass transport as well as in TW temperature (18.59, 18.23 and 18.05°C). The freshwater flux of the AC presents low values (-0.04 ± 0.01, -0.02 ± 0.01 and -0.02 ± 0.01 Sv), associated to similar TW salinities among decades (36.258, 36.377 and 36.359).

370 Our results show relatively strong values for the AC (**Figures 2 and 3**), similar to the values obtained by Hernández-Guerra et al. (2014). However, historical estimations place the average AC transport in a range between 2-12 Sv (Lee et al., 1996; Olson et al., 1984; Schmitz et al., 1992; Schmitz and McCartney, 1993). More recently, a combination of different observation systems at 26.5°N from 2005 to 2015 shows a relatively weak AC of 4.7 Sv with a daily standard deviation of 7.5 Sv (Meinen et al., 2019), with transports varying between -15 and 25 Sv (Johns et al., 2008), despite presenting a rather

375 weak seasonal component (Meinen et al., 2019).

3.1.8 Canary Current

The Canary Current (CC) is the relatively weak eastern boundary current of the North Atlantic subtropical gyre, linking the Azores Current with the North Equatorial Current (Pérez-Hernández et al., 2013; Casanova-Masjoan et al., 2020; Comas-Rodríguez et al., 2011). The CC flows along the first ~750 m of the water column (Pérez-Hernández et al., 2013; Hernández-

380 Guerra et al., 2017; Casanova-Masjoan et al., 2020) from the surface to 27.23 kg m^{-3} and with a width over ~270 km (**Figure 6 h, i** and **Table 2**). The different geographical position of the stations at this boundary for the cruise carried out during 1990-99 prevents from obtaining values directly comparable to the other estimates. At these latitudes there is a point of inflection in the accumulated mass transport denoting the start of the CC, from non-significant values to negative mass transport. This current transports southward -5.1 ± 0.9, -6.1 ± 1.4 and -4.8 ± 0.7 Sv of mass (**Figure 2**), -0.34 ± 0.06, -0.40 ±

0.08 and -0.32 ± 0.05 PW of heat (**Figure 3**) and 0.01 ± 0.01, 0.03 ± 0.01 and 0.01 ± 0.01 Sv of freshwater (**Figure 4**). Moreover, this current carries waters with TW temperatures lower than its western counterpart (16.57, 16.59 and 16.86°C) and similar high TW salinities (36.283, 36.313 and 36.372).

The CC has an average transport of -3.0 ± 1.0 Sv with a seasonal amplitude of 1.4 ± 0.7 Sv (Machín et al., 2006; Pérez-Hernández et al., 2023). The CC varies seasonally not only in intensity but also in position, migrating from its easternmost location in spring to its westernmost point in fall. Our estimations are nearly double the results obtained by Hernández-Guerra et al. (2014) for the same cruises of 2.1 ± 0.9 Sv for 1992 and 2.3 ± 1.1 Sv for 2011 between the eastern boundary and 20°W, or the 2.9 ± 0.8 Sv of Machin et al. (2006). Nevertheless, most of the previous CC observations have taken place in fall when the transports have been observed to be as high as -6.2 ± 0.6 Sv with a northward recirculation in the Lanzarote Passage (Pérez-Hernández et al., 2013; Hernández-Guerra et al., 2017).

East of the CC, the Lanzarote Passage presents a unique dynamic, with its own pattern of variability that has been related to the seasonal amplitude of the AMOC (Pérez-Hernández et al., 2015; Vélez-Belchí et al., 2017; Pérez-Hernández et al., 2023). Our results for the cruises carried out during 2000-09 and 2010-19 have found -1.0 ± 0.6 and -1.8 ± 0.6 Sv over ~70 km, respectively, carrying waters with similar TW temperature and salinity. These values correspond to the spring-summer estimates for the Lanzarote passage flow of -0.81± 1.48 Sv estimated with nine years of mooring data (Casanova-Masjoan et al., 2020; Fraile-Nuez et al., 2010).

3.1.9 Gulf Stream

The strong Gulf Stream (GS) brings warm water from the Gulf of Mexico into the North Atlantic subtropical gyre including water from the FC and AC (**Figures 2 and 3**). After the GS turns offshore from the continental shelf at Cape Hatteras, the mass transport carried by the GS nearly doubles at a rate of 8 Sv every 100 km, with large variations in space and time (Johns et al., 1995; Hogg and Johns, 1995; Frankignoul et al., 2001). The section at 36°N sampled during the 2000-09 decade can detect its strength along the coast, occupying the first ~900 m of the water column (up to 27.84 kg m^{-3}) and with a horizontal extension over ~250 km from 71.7°W to 69.1°W. The GS has a strong northward transport of 74.9 ± 1.7 Sv for mass and 4.56 ± 0.11 PW for heat, as well as strong southward freshwater flux of -0.82 ± 0.04 Sv (**Figure 6 e, f** and **Table 2**). McDonagh et al. (2010) found similar values of 67.2 ± 17.2 Sv for the GS transport at 36°N, and Rossby et al. (2014) detected no significant trends in the strength of the GS surface transport over the last 20 years using direct measurements. Almost half of the northward transport associated to the GS is recirculated southward, up to 64.8°W (387 km east to the east of the GS). This recirculation of the GS brings southward -35.4 ± 8.7 Sv of mass transport and -2.29 ± 0.18 PW of heat transport, with an opposing freshwater flux of 0.19 ± 0.05 Sv.

The GS presents high TW temperature (15.42°C), but not as high as for the FC and AC, and a similar value of TW salinity (36.014) compared with FC and AC.

3.1.10 North Atlantic Current

The North Atlantic Current (NAC) is a variable wind-driven body of warm water covering a large part of the eastern subpolar North Atlantic (SPNA) on its way to the Nordic Seas. The NAC represents the bulk of the GS after its branch point and subsequent separation from the coast (**Figure 2**). The NAC at 47°N is located between 49.6°W and 44.4°W for the 1990-99 cruise and between 42.9°W and 39.0°W for the 2010-19 cruise, due to the difference in the geometry of the two cruises, reaching similar depths of 838 and 982 m from 26.45 to 27.23 kg m^{-3}, respectively. The mass transports for NAC at 47°N are consistent with those of the net GS system after considering its recirculation, the small contribution that recirculates within the subtropical gyre (see Canary Current) and the -1.9 ± 2.3 Sv and -1.3 ± 2.1 Sv that sink between the 24°N and 47°N sections for each decade, respectively (Caínzos et al., 2022). Thus, the NAC transports 33.4 ± 2.9 and 28.2 ± 1.5 Sv in the solutions for the 1990-99 and 2010-19 decades, respectively (**Figure 6 c, d** and **Table 2**). The main mass transport is subsuperficial with a mass transport of 21.7 ± 2.0 and 17.3 ± 0.8 Sv in the layer between 26.45 (~200 m) and 27.23 kg m^{-3} (~400 m) in 1990-99 and 2010-19, respectively. Meinen and Watts (2000) using current meter moorings and IES attributed a much higher value of 146 ± 13 Sv for the NAC at 42°N for the whole water column, located close to our hydrographic section at 47°N carried out during 1990-99. A more recent study combining altimetry and Argo data reconstructed the transports of NAC from 1993 to 2016 between 40°N and 53°N, attributing values between 35 and 50 Sv along 47°N between 45°W and 37°W (Stendardo et al., 2020). Our estimations for heat transport are lower than those of the GS (1.79 ± 0.14 and 1.18 ± 0.05 PW, respectively), due to the reduction in the TW temperature (13.53 and 10.59°C) on its way northward. The freshwater flux has also been reduced (-0.22 ± 0.04 and -0.09 ± 0.02 Sv), resulting from the lower values in TW salinity (35.722 and 35.368).

The NAC flows northeastward and reaches the section at 58°N (**Figure 6 a, b, Figure 7 f** and **Table 2**). At this latitude, the NAC extends longitudinally between 21.7°W and 14.1°W, 22.8°W and 13.2°W and 21.1°W and 10.1°W for each of the three cruises within the 1990-99, 2000-09 and 2010-19 decades, respectively, with a vertical extension from the surface to 27.84 kg m^{-3} (~1000 m). The strength of the current has been largely reduced at this point, with net mass transports of 5.2 ± 3.7, 5.4 ± 2.7 and 6.7 ± 1.6 Sv (**Figure 2**) and heat transport of 0.19 ± 0.13, 0.20 ± 0.10 and 0.25 ± 0.05 PW (**Figure 3**). This corresponds to a 20 to 25-Sv reduction in the transport of the NAC crossing the SPNA, with near a fifth part corresponding to a sink in these latitudes (3.8 ± 3.1 Sv between 47°N and 55°N, 4.8 ± 2.7 Sv between 36°N and 55°N and 4.0 ± 2.4 Sv between 47°N and 55°N (Caínzos et al., 2022).

Stendardo et al. (2020) found an average value of 2.5 Sv for the NAC at this latitude, which is slightly lower than our estimations. Moreover, recent glider sections from July 2014 to August 2016 along 58°N from 21°W to 15°W (Houpert et al., 2018) over the Rockall Trough branch have provided a year mean absolute geostrophic mass transport of 5.1 ± 1.0 Sv, with 6.7 ± 0.9 Sv for summer and 2.8 ± 1.7 Sv for winter, comparable to our estimations at 58°N.

The freshwater flux at this latitude is almost negligible (0.03 ± 0.02, 0.00 ± 0.01 and -0.01 ± 0.01 Sv). Both TW temperature and salinities have become colder and fresher, with quite stable values for both properties (9.12, 9.27 and 9.29°C for the TW temperature and 35.290, 35.347 and 35.292 for the TW salinity).

3.1.11 East Reykjanes Ridge Current, Irminger Current and East Greenland Current

The surface currents on the eastern part of the northernmost section, at the nominal latitude of 58°N, are an important link between the Arctic Ocean and the North Atlantic Ocean via their upper circulation (**Figure 1**). Within the Iceland Basin, the NAC flows cyclonically turning southwestward and flowing along the Reykjanes Ridge flank as the East Reykjanes Ridge Current (ERRC), that then turns anticyclonically around and across the ridge (Pollard et al., 2004). Thus, upon entering the Irminger Sea, the Irminger Current (IC) flows northward along the western flank of the Reykjanes Ridge carrying warm, saline Atlantic waters. Petit et al. (2019) have described the along-stream evolutions of the structure and properties of the ERRC and IC. They found interconnections between both flows governed by the complex bathymetry of ridges and basins. The ERRC runs along the eastern side of the Reykjanes Ridge and Iceland over ~80 km, exporting waters southward in the upper layers up to 27.84 kg m^{-3} (~1000 m deep), with relatively high values of TW temperature and salinity (**Figure 7 e, g** and **Table 2**). We have found low values of mass transport for the southward flowing ERRC (-3.2 ± 2.2, -1.8 ± 1.4 and -2.0 ± 0.8 Sv for each cruise, respectively; **Figure 2**). Using repeated ship-based measurements along the Greenland-Portugal OVIDE line, Daniault et al. (2016) have estimated the decadal mean circulation for the North Atlantic over 2002-2012, with values for the ERRC transport slightly larger than ours (-4.1 ± 0.6 Sv). The associated heat transport is quite small (-0.10 ± 0.07, -0.06 ± 0.04 and -0.06 ± 0.02 PW; **Figure 3**), and the freshwater flux is null (0.00 ± 0.01 Sv for all cases; **Figure 4**). The TW temperatures (8.14, 8.45 and 7.79°C) and salinities (35.131, 35.070 and 35.082) are slightly lower than those of NAC.

On the other side of the Reykjanes Ridge, the ~300 km-wide IC transports waters from the SPNA toward the Arctic Ocean in the upper ~700 m, with a shallowing of the 27.84 kg m^{-3} isopycnal (**Figure 7 d, g** and **Table 2**). The northward transport of mass (5.0 ± 2.7, 4.7 ± 1.9 and 6.1 ± 1.2 Sv; **Figure 2**) agrees with the result obtained by Daniault et al. (2016; 4.8 ± 1.1 Sv) and Sarafanov et al. (2012; 5.6 ± 0.4 Sv). Casanova-Masjoan et al. (2020) obtained 3.04 ± 0.23 Sv for the Irminger current around Iceland, of which 2.24 ± 0.23 Sv flow north as part of the North Icelandic Irminger Current (NIIC). However, other studies have attributed IC transports in the range of 9-12 Sv (Våge et al., 2011b; Lherminier et al., 2010; Bacon, 1997). There is also a northward transport of heat (0.13 ± 0.06, 0.15 ± 0.05 and 0.17 ± 0.03 PW), although with null values for the freshwater flux. The values of TW temperature (6.37, 8.12 and 6.91°C) and salinity (34.991, 35.105 and 35.019) are, again, slightly lower than those from the ERRC.

Flowing southward along the eastern coast of Greenland, the East Greenland Current (EGC) exports cold and fresh water from the Arctic into the SPNA (**Figure 7 c, g** and **Table 2**). The values of net southward mass transport are small but strengthen with time (-0.4 ± 0.6, -1.6 ± 1.8 and -3.3 ± 1.0 Sv; **Figure 2**), with almost null heat transports (-0.01 ± 0.01, -0.04 ± 0.04 and -0.06 ± 0.02 PW; **Figure 3**) and null freshwater flux (**Figure 4**). We have found variable transports for the EGC,

480 relatively weaker than previous estimations (-3.8 ± 0.3 Sv from Daniault et al., 2016; -5.4 ± 0.7 from Sarafanov et al., 2012; and -3.5 ± 0.5 Sv le Bras et al., 2018). The TW temperatures (5.94, 6.60 and 4.42°C) and salinities (34.938, 34.826 and 34.560) show the lower values found in the upper layers of the 58°N section.

3.1.12 Upper West Greenland Current and upper Labrador Current

The EGC turns northwest at the southern tip of Greenland, entering the Labrador Sea and originating the upper West
485 Greenland Current (uWGC) at 53°N. The uWGC varies horizontally, ranging from the coast to 49.0°W (67 km), 49.9°W (164 km) and 47.4°W (75 km) for each decade, as well as vertically (from the surface to 262, 1232 and 788 m). The waters entering the Labrador Sea have a small but variable net transport for mass (1.3 ± 0.4, 1.6 ± 1.0 and 3.4 ± 1.0 Sv; **Figure 2**), with an intensification for the last cruise studied (**Figure 7 b, g** and **Table 2**). These values are lower than the average transports of uWGC estimated previously: 3.8 ± 0.9 Sv (Myers et al., 2007) at Cape Farewell; 3.2 ± 2.3 Sv and 5.5 ± 3.9 Sv
490 at Cape Farewell and Cape Desolation, respectively (Myers et al., 2009) and 4.6 Sv at both Cape Farewell and Cape Desolation (Gou et al., 2022). More recent estimations have situated the upper transport via the eastern basin of the Labrador Sea in 11.1 ± 5.0 Sv (Pacini et al., 2020). The values for heat (0.01 ± 0.01, 0.03 ± 0.02 and 0.05 ± 0.02 PW; **Figure 3**) and freshwater (0.01 ± 0.01, 0.00 ± 0.01 and 0.04 ± 0.01 Sv; **Figure 4**) transports are negligible except for the last estimate. These values can reflect the mean value obtained from seven decades of high-resolution coupled ice-ocean model results,
495 with mean annual fluxes between 99 and 162 mSv (Florindo-López et al., 2020). The TW temperatures (2.74, 4.62 and 3.57°C) and salinities (34.126, 34.857 and 34.332) have yet again become colder and fresher.

The net export of the water formed in the Labrador Sea is through its southwestern border, as part of the Labrador Current (LC). The net transport can be divided into the upper and deep layer, setting the interface at a neutral density of 27.84 kg m^{-3}, up to a depth of ~400 m. The upper LC extends from 54.3°W to 54.1°W, 54.8°W to 54.1°W and 54.2°W to 52.1°W,
500 occupying 26, 80 and 151 km. The upper layers of the LC transport out of the Labrador basin -2.1 ± .05, -1.2 ± 0.4 and -1.6 ± 0.4 Sv of mass transport (**Figure 2**), with null values for either heat or freshwater flux (**Figure 7 a, g** and **Table 2**). This southward export is lower than estimations from mooring data (-6.3 ± 0.2 Sv 10-year mean by Fischer et al., 2010; -8.3 ± 0.5 Sv 17-year mean by Zantopp et al., 2017) and hydrographic sections (-6.3 Sv mean over 1996-2003 by Li and Lozier, 2018). The TW temperatures in this upper layer are very cold (0.45, 0.98 and 0.22°C), associated with low salinities (33.569,
505 33.630 and 33.455).

3.2 Deep currents

3.2.1 Iceland-Scotland Overflow Waters and Denmark Strait Overflow Waters

The deep layers of the east part of the northernmost section (at 58°N) constitute the overflow waters, divided into the Iceland-Scotland Overflow Waters (ISOW) and the Denmark Strait Overflow Waters (DSOW). The ISOW flows between
510 the Scottish and Icelandic platforms, exporting water from the Arctic into the Atlantic from ~2100 m to the bottom of the

water column. The longitudinal extension of the ISOW is similar for all decades (335 km from 28.9 to 23.3°W, 567 km from 33.9 to 24.6°W and 416 km from 31.3 to 24.4°W for the cruises carried out during 1990-99, 2000-09 and 2010-19, respectively; **Figure 7 l, m** and **Table 3**). There is a net southward transport of -10.8 ± 6.5, -9.6 ± 5.3 and -10.0 ± 3.0 Sv of mass across those longitudes (**Figure 2**), accompanied by a southward transport of heat (-0.13 ± 0.09, -0.11 ± 0.07 and -0.12 ±0.04 PW; **Figure 3**). Our results can be overestimated due to the low values of southward transport for both EGC and ERRC. Previous estimations for ISOW are considerably weaker than our results. García-Ibáñez et al. (2015) built an inverse model for the SPNA discussing the contributions from source water masses, estimating for deep layers -1.4 ± 1.0 Sv of ISOW being exported out of the eastern North Atlantic. Moreover, using an array of current meters deployed as part of the OSNAP program, Johns et al. (2021) have determined a mean southward flow of ISOW along the eastern flank of the Reykjanes Ridge of -5.3 ± 0.4 Sv between 2014-2018. The TW temperatures (3.07, 3.04 and 3.08°C) and salinities (34.943, 34.944 and 34.958) are quite stable among decades.

The DSOW has been divided into two main paths, flowing along the boundaries of the Irminger Sea. The DSOW flowing at the western side of the Reykjanes Ridge (eastern boundary of Irminger Sea) extends ~110 km between 37.2°W and 36.1°W, 37.8°W and 35.9°W and 37.7°W and 35.3°W for each inverse solution, respectively (**Figure 7 k, m** and **Table 3**). This path of the DSOW exports between ~2500 m and the bottom layers -3.7 ± 8.2, -2.4 ± 8.0 and -0.9 ± 4.6 Sv of mass transport per decade (**Figure 2**), with low associated heat transports (-0.05 ± 0.10, -0.03 ± 0.10 and -0.02 ± 0.06 PW; **Figure 3**). The TW temperatures are slightly higher than those of ISOW (3.28, 3.50 and 4.27°C), but with lower salinities except for the last estimate (34.886, 34.908 and 34.955).

The western branch of the DSOW extends over ~180 km from the coast and from ~2000 m to the bottom of the water column. This current flowing along the western boundary of the Irminger Sea (**Figure 7 j, m** and **Table 3**) has a slightly stronger export of water southwards (-4.9 ± 7.8, -5.5 ± 6.8 and -6.2 ± 4.9 Sv; **Figure 2**), with similarly low values of heat transport (-0.04 ± 0.10, -0.05 ± 0.09 and -0.06 ± 0.07 PW; **Figure 3**) and null freshwater flux (**Figure 4**). The TW temperatures (2.29, 2.45 and 2.54°C) are lower than on the western boundary of the Irminger Sea, while maintaining similar TW salinities (34.904, 34.911 and 34.915).

The combined values for both paths of DSOW exceed the year-long mean total volume transport of DSOW upstream of our section. Hydrographic sections over different summers at the Denmark Strait yielded -4.9 ± 0.5 Sv southward (Brearley et al., 2012), while mooring arrays at the northern part of the Denmark Strait estimated -3.54 ± 0.16 Sv (Harden et al., 2016), similar to results from downstream the sill (3.4 Sv with a standard deviation of 1.4 Sv, Jochumsen et al., 2012). This increase in DSOW southward of the Denmark Strait may respond to the entrainment of water from the Irminger Current, nearly doubling the volume transport carried by the DSOW (Koszalka et al., 2013; Dickson et al., 2008).

3.2.2 Deep West Greenland Current and deep Labrador Current

Analogously to the uWGC, there is a northward deep transport entering the Labrador Sea via its eastern boundary, the deep West Greenland Current (dWGC) occupying ~220 km from the coast to the interior of the Labrador Sea and flowing along

the lower part of the water column (from ~3500 m to the bottom). This current carries into the Labrador basin 5.4 ± 1.0, 5.8 ± 1.1 and 8.8 ± 1.5 Sv of mass transport (**Figure 2**) for the cruises within 1990-99, 2000-09 and 2010-19, respectively (**Figure 7 i, m** and **Table 3**). This last value is comparable with the 8.3 ± 2.8 Sv found by Pacini et al. (2020) using high-resolution moorings from 2014 to 2018 deployed as part of OSNAP. The increase in transport for the last estimate is also evident for heat transport (0.04 ± 0.01, 0.04 ± 0.01 and 0.07 ± 0.01 PW; **Figure 3**), with null freshwater flux (**Figure 4**). The dWGC is slightly colder (TW temperatures of 1.84, 1.93 and 2.04°C) and saltier (TW salinities of 34.900, 34.888 and 34.908) than the uWGC, with lower temperature and salt content than the western branch of the DSOW.

Deep layers export most of the LC out of the Labrador Sea through its western boundary. It is a relatively narrow current, extending over 364, 89 and 424 km, with its upper vertical interface ranging from 2615, 1956 and 2314 m deep to the bottom for each decade. This outflow of mass transport increases with time (-5.2 ± 0.9, -8.4 ± 3.9 and -11.4 ± 6.8 Sv; **Figure 2**), although not significantly, due to the high variability associated to the deep LC, expressed with the large values of uncertainties, around half of the mean value (**Figure 7 h, m** and **Table 3**). However, other studies have found stronger deep-water transports: 26 ± 5 Sv from two years of direct current observations and moored current-meter array (Fischer et al., 2004), updated to 30 ± 3 Sv for the 10-year mean (Fischer et al., 2010) and an average of 30.2 ± 6.6 Sv over the past 17 years from moorings and shipboard station data (Zantopp et al., 2017). These differences may arise due to the strong barotropic component observed for this current that inverse solutions fail to resolve. Heat is also exported out of the Labrador Sea via deep layers, with values of -0.04 ± 0.01, -0.07 ± 0.05 and -0.11 ± 0.09 PW for each decade (**Figure 3**), respectively. Freshwater fluxes remain almost negligible. The TW temperatures and salinities are warmer (1.92, 2.24, 2.37°C) and saltier (34.900, 34.893 and 34.911) than for upper layers, with values similar to those of the western DSOW.

3.2.3 Deep Western Boundary Current

The Deep Western Boundary Current (DWBC) mainly follows the western border of the Atlantic Ocean. The DWBC at 47°N lies below the neutral density of 27.84 kg m^{-3} (~2800 m to the bottom) and occupies a similar longitudinal extension to the upper northward NAC (~280 km) (**Figure 8 a, b** and **Table 3**). The DWBC flows southward at 47ºN with a mass transport of similar magnitude (-30.1 ± 10.4 and -37.5 ± 5.7 Sv for the cruises carried out during 1990-99 and 2010-19, respectively; **Figure 2**). These values for the DWBC exceed the -17.5 Sv estimated by Fischer et al. (2015) at Grand Banks with ADCP velocities. The DWBC at this latitude also transports a southward heat transport (-0.31 ± 0.13 and -0.34 ± 0.07 PW; **Figure 3**) with null values of freshwater flux. The DWBC presents TW temperatures of 2.64 and 2.30°C and TW salinities of 34.922 and 34.909.

The DWBC at 36°N (**Figure 8 c, d** and **Table 3**) gets wider, occupying 406 km from the coast to 67.3°W while flowing along similar depth levels (from ~2682 m to the bottom). The net mass transport of -34.5 ± 8.7 Sv is southward (**Figure 2**), similar to the estimate for the 2000-09 decade at 47°N, associated with -0.29 ± 0.10 PW of heat transport (**Figure 3**), in agreement with the 10-year mean of -29.59 ± 2.08 Sv from the mooring line W. The values for the TW properties are quite similar to those at 47°N (2.13°C for TW temperature and 34.906 for TW salinity).

The presence of Antarctic Bottom Water (AABW) at 24.5°N constitutes a deep boundary for the vertical extension of the DWBC, that is, therefore, restricted to neutral densities between 27.84 and 28.23 kg m^{-3} (from ~2500 m to ~5500 m deep). At this latitude, we find even wider (and varying) horizontal extensions of the DWBC, ranging between 1062, 601 and 1663
580 km for each decade, from the coast to 62.7°W, 56.9°W and 54.6°W (**Figure 8 e, f** and **Table 3**). The strength of the DWBC has decreased when it reaches this latitude, with mass transports of -23.8 ± 10.8, -18.3 ± 9.8 and -30.4 ± 7.3 Sv for each cruise, respectively (**Figure 2**). These values, with their relatively large uncertainties, coincide with the IES-derived transport from Meinen et al. (2004; -25 ± 9 Sv), and with the mooring array estimations from Johns et al. (2008; -26.5 Sv), as well as inverse solutions using hydrography from Hernández-Guerra et al. (2014; -22.1 ± 4.2 for the 1992 cruise and -20.1 ±
585 3.7 Sv for the 2011 cruise). The heat transport is also reduced (-0.27 ± 0.11, -0.22 ± 0.10 and -0.33 ± 0.07 PW; **Figure 3**), while the freshwater remains negligible. The TW properties become warmer (2.88, 3.10 and 2.72°C) and saltier (34.954, 34.963 and 34.941) on its way south. West of the DWBC there is a recirculation that carries water northward at deep layers, previously estimated to be around 13 Sv using current metre moorings (Bryden et al., 2005a) and 8 Sv from CTD and LADCP profiles (Biló and Johns, 2020), despite the poorly defined zonal extent of the circulation.
590 The distribution of AABW into the South Atlantic constitutes a deep boundary for the vertical extension of the DWBC, that is shifted upwards between neutral densities of 27.58 and 28.15 kg m^{-3}. At 11°S for the cruise carried out during the 1990-99 decade, the DWBC flows as a narrow jet along the coast up to 35.1°W (~88 km wide), extending from ~1323 to ~2561 m in the water column (**Figure 8 g, h** and **Table 3**). This deep southward flow transports -17.3 ± 2.2 Sv of mass (**Figure 2**), -0.23 ± 0.03 PW of heat (**Figure 3**) and 0.02 ± 0.01 Sv of freshwater (**Figure 4**). Hummels et al. (2015) found similar values of
595 DWBC transport from shipboard and moored observations (-17.5 ± 1.7 Sv), while previous studies using hydrographic sections and ADCP velocity measurements have obtained much stronger southward transports (-35.5 ± 14.7 Sv; Schott et al., 2005). While the TW temperature has increased on its way south (3.39°C), the DWBC has become fresher (TW salinity of 34.902).

The DWBC at 19°S for the cruise contained in the 1990-99 solution has extended horizontally to a width of 168 km (from
600 the coast to 35.8°W) and deepened (between 1493 and 3370 m). The deep current at this latitude has increased its southward mass transport to -20.8 ± 7.2 Sv (**Figures 2, 8 i, j** and **Table 3**), as well as heat (-0.25 ± 0.09 PW; **Figure 3**). The water mass has become colder but saltier, with a TW temperature of 2.98°C and TW salinity of 34.927.

On its way southward, the DWBC gets wider until reaching values of 808 and 967 km at 24°S for the cruises carried out during 2000-09 and 2010-19, respectively, while occupying similar vertical depths (from ~1400 to ~3000 m) (**Figure 8 k, l**
605 and **Table 3**). At 24°S, the DWBC transports -29.0 ± 9.0 and -27.5 ± 7.1 Sv of mass southward for the cruises within the 2000-09 and 2010-19 models (**Figure 2**), respectively, with a more intense DWBC than in other inverse solutions (Arumí-Planas et al., 2023). This deep transport has increased with respect to 19°S, not only in mass but also in heat (-0.33 ± 0.10 and -0.32 ± 0.08 PW; **Figure 3**), with an almost null freshwater flux (0.02 ± 0.01 and -0.02 ± 0.01 Sv; **Figure 4**). At this latitude, the DWBC gets colder but also fresher, with TW temperatures of 2.92 and 2.91°C and TW salinities of 34.891 and
610 34.786.

When the DWBC reaches 30°S, its location presents certain variability, ranging between 443, 282 and 833 km wide, and between depths of 1336 to 2177 m, 1674 to 2861 m and 1368 to 2580 m in 1990-99, 2000-09 and 2010-19, respectively (**Figure 8 n, o** and **Table 3**). However, the strength of the southward deep current is quite similar to the values at 24°S, and they are quite stable among decades. The net mass transports of the DWBC at 30°S are -26.6 ± 5.1, -25.9 ± 5.0 and -27.9 ±

615   1.9 Sv for each cruise (**Figure 2**), significantly higher than previous estimations of -16.1 ± 5.1 Sv using hydrography (Hernández-Guerra et al., 2019). The heat transports associated to the DWBC at this latitude remain similar with time (-0.32 ± 0.06, -0.32 ± 0.06 and -0.32 ± 0.02 PW; **Figure 3**), with almost null freshwater fluxes (0.02 ± 0.01, -0.01 ± 0.02 and 0.01 ± 0.01 Sv; **Figure 4**). The TW temperatures have increased (3.06, 3.11 and 2.93°C), while reducing the values of the TW salinities (34.820, 34.830 and 34.840).

620   The southernmost section of our study, at 45°S, manifests the presence of a narrow DWBC (162 km) from 57.8°W to 55.8°W (**Figure 8 q, r** and **Table 3**), occupying a significant larger part of the water column (~717 to ~3352 m). There is a strong DWBC transport of -49.1 ± 7.0 Sv for mass, -0.53 ± 0.07 PW for heat and -0.20 ± 0.04 Sv for freshwater. The DWBC at this latitude has gotten colder (TW temperature of 2.73°C) and fresher (TW salinity of 34.265).

3.2.4 Deep Eastern Boundary Current

625   The change in the orientation of the Brazilian coast after Cape São Roque (**Figure 1**) results in a division of the main DWBC that originates an eastern branch that crosses the Mid Atlantic Ridge (MAR). In our hydrographic sections, the separate branch of the DWBC lies on the eastern side of the MAR at 24°S, and it has been denominated the Deep Eastern Boundary Current (DEBC; Arhan et al., 2003; Bower et al., 2019; Garzoli et al., 2015; Stramma and England, 1999).

The DEBC at 24°S covers a horizontal range of ~420 km and a vertical range between ~1400 and ~4100 m for the cruise

630   carried out during the 2000-09 decade and ~1400 and ~5100 m for the one during the 2010-19 decade. The mass transport carried out by the DEBC at 24°S for the both cruises is quite variable, with net mass transports of -13.7 ± 5.5 and -9.7 ± 6.1 Sv, respectively (**Figures 2, 8 l, m** and **Table 3**), not significantly different than the estimation from Arumí-Planas et al. (2023) of -16.3 ± 4.7 Sv. The heat transport values are quite similar (-0.14 ± 0.05 and -0.12 ± 0.06 PW; **Figure 3**) despite the variable mass transports, due to the differences in the TW temperatures (2.59 and 3.03°C). The TW salinities have values of

635   34.829 and 34.786 with a null value of freshwater flux.

At 30°S the DEBC occupies a smaller part of the water column, between ~2500 and ~3800 m deep, with a horizontal extension of ~900 km wide (**Figure 8 o, p** and **Table 3**). This southward flow exhibits similar values of mass transport among decades (-8.3 ± 4.6, -9.7 ± 3.5 and -8.6 ± 3.4 Sv for each of the three cruises carried out within the 1990-99, 2000-09 and 2010-19 decades, respectively; **Figure 2**), reproduced for heat transport (-0.08 ± 0.05, -0.09 ± 0.03 and -0.08 ± 0.03 PW;

640   **Figure 3**). Hernández-Guerra et al. (2019) found similar values for the 2003 and 2011 cruises (-8.2 ± 5.6 Sv and -12.7 ± 5.5 Sv, respectively), comparable with the IES reconstruction of -12 Sv from Kersalé et al. (2019). The values for the TW properties remain quite stable in time, for both temperature (2.48, 2.44 and 2.31°C) and salinity (34.828, 34.833 and 34.852).

The 45°S section exhibits the presence of a narrower (415 km) DEBC for the 1990-99 solution, from 10.9°E to 14.6°E (**Figure 8 r, s** and **Table 3**). There is a reduction in the southward transport of mass (-6.4 ± 6.3 Sv; **Figure 2**) and heat (-0.06 ± 0.06 PW; **Figure 3**) compared with the values at 30°S, carrying waters with TW temperature of 2.22°C and TW salinity of 34.860.

3.3 Bottom currents

3.3.1 Antarctic Bottom Water

The Antarctic Bottom Water (AABW) originates in the Southern Ocean and reaches the Atlantic Ocean as the densest water mass, distributing along the ocean bottom on its way northward. At 45°S, the AABW enters the Atlantic Ocean west of the MAR between 57.4ºW and 17.4ºW, from ~3800 m to the bottom for the cruise carried out during the 1990-99 decade, introducing a net mass transport of 4.7 ± 1.7 Sv (**Figure 2**) of cold (TW temperature of 0.41°C) and relatively fresh (TW salinity of 34.697) water (**Figure 9 m, n** and **Table 4**). No heat or freshwater transport is associated to the AABW. Previous studies using the same hydrographic section have found similar net inputs from the AABW at the Argentine Basin (5.6 ± 1.0 Sv by McDonagh and King, 2005 and 5.6 ± 0.9 Sv by Naveira Garabato et al., 2014). East of the MAR, there is another contribution from the Southern Ocean to the South Atlantic basin (**Figure 9 n, o** and **Table 4**). However, including its recirculation, the net transport yields a southward -0.9 ± 1.6 Sv of water slightly warmer and saltier (TW temperature of 1.18°C and TW salinity of 34.777). Therefore, the total net transport of bottom waters at 45°S introduces 3.8 ± 1.7 Sv into the Atlantic basin.

The AABW continues its way to the north and reaches 30°S west of the MAR between 45.7°W and 17.7°W, 45.7°W and 19.0°W and 45.4°W and 18.2°W for the cruises solved within the 1990-99, 2000-09 and 2010-19 models, respectively (**Figure 9 j, k** and **Table 4**), occupying the water column at depths below ~3500 m. The net strength of the Western AABW has reduced at this point, with quite stable values in time for mass transport (3.9 ± 1.3, 3.3 ± 1.3 and 3.5 ± 1.5 Sv; **Figure 2**). The TW temperatures (0.46, 0.71 and 0.55°C) and salinities (34.722, 34.750 and 34.730) of this water mass at this latitude west of the MAR have increased, after being mixed with the water masses above while flowing northward, with marked higher values for the cruise obtained during the 2000-09 period. The eastern AABW yields non-significant values for the mass transport at any decades (-0.3 ± 1.0, 0.1 ± 1.0 and 0.5 ± 0.9 Sv; **Figure 9 k, l** and **Table 4**), due to the blockage of northward flowing AABW by the Walvis Ridge (**Figure 1**). As a result, the net total transport across bottom layers is dominated by the western subbasin (3.5 ± 1.2, 3.4 ± 1.4 and 4.1 ± 1.5 Sv). Results from previous studies attribute similar albeit slightly stronger AABW northward transports at 30°S, with 5.4 ± 1.4 Sv (McDonagh and King, 2005) and 5.2 ± 1.1 Sv (Naveira Garabato et al., 2014) for the 1992-93 cruise and 6.5 ± 1.9 Sv and 8.3 ± 2.1 Sv for the 2003 and 2011 cruises, respectively (Hernández-Guerra et al., 2019).

The AABW at 24°S occupies smaller horizontal extensions west of the MAR, from 38.0°W to 17.0°W (2138 km) and from 38.0°W to 14.8°W (2362 km) for the cruises carried out during the 2000-09 and 2010-19 decades, respectively (**Figure 9 g,**

675 **h** and **Table 4**). At this latitude, the upper level of the AABW has deepened to ~4550 m. The values for the last two estimates at 24°S show weaker AABW mass transports west of the MAR (0.5 ± 2.3 and 1.9 ± 2.0 Sv; **Figure 2**). The eastern basin shows similar values to the western basin, with inputs of 1.0 ± 2.0 and 0.3 ± 1.4 Sv (**Figure 9 h, i** and **Table 4**). The total AABW transports (1.5 ± 1.4 and 2.2 ± 1.5 Sv) yield lower results than other inverse solutions for the 2009 cruise (2.6 ± 0.5 Sv; Evans et al., 2017) and 2018 cruise (6.6 ± 1.6 Sv; Arumí-Planas et al., 2023).

680 Following its way northward along the South American coast, the AABW at 19°S can be found between 37.4°W and 19.2°W (1914 km wide) in the horizontal and between ~4260 m and the bottom of the ocean (**Figure 9 e, f** and **Table 4**). At this latitude, no eastern contribution can be found and the AABW is restricted west of the MAR. The AABW at 19°S shows similar values of mass transport (1.9 ± 1.4 Sv; **Figure 2**) for the first estimate to the total values at 24°S for the cruises obtained during the following decades (2000-09 and 2010-19).

685 The AABW at 11°S appears between 35.2°W and 17.0°W, occupying ~1900 km in the horizontal, and in the vertical from 4377 m to the bottom of the water column (**Figure 9 c, d** and **Table 4**). The strength of the AABW flow at 11°S remains mainly unchanged (1.2 ± 1.2 Sv of mass transport; **Figure 2**). Using a combination of shipboard measurements and mooring arrays, Schott et al. (2005) have estimated a mean northward transport of 2.7 ± 2.9 Sv over 2000-04, which yield similarly non-significant values.

690 The last section where we can observe the presence of the AABW is 24.5°N, with relatively large horizontal extensions (75.5°W to 54.7°W, 76.8°W to 53.7°W and 76.9°W to 52.3°W of 2103, 2322 and 2474 km wide, respectively) with very small mass transports (0.1 ± 0.9, 0.7 ± 0.9 and 0.3 ± 1.3 Sv; **Figure 2**) for the cruises carried out during 1990-99, 2000-09 and 2010-19 (**Figure 9 a, b** and **Table 4**). Comparable non-significant northward mass transports are obtained by Hernández-Guerra et al. (2014) for 1992 (1.4 ± 1.8 Sv) and 2011 (1.1 ± 1.8 Sv). The combination of shipboard 695 measurements and the RAPID mooring array yield similar weak AABW transports, with mean values of 1.0 Sv (McCarthy et al., 2015) and stronger ranges of 2.2-3.7 Sv (Frajka-Williams et al., 2011).

4 Summary and conclusions

The complex system of currents throughout the Atlantic basin that constitute the AMOC has been described in this study using repeated hydrographic sections over the last thirty years. Inverse methods enable quantifying not only the AMOC, but 700 also the strength and properties associated with the most significant currents flowing along the Atlantic Ocean, attending to their transports of mass, heat, and freshwater for different vertical and horizontal ranges. All uncertainties quoted are formal results that depend on the limited assumptions imposed on the inverse model and should not be regarded as strictly limiting the total strength of these time mean currents.

Surface currents in the subtropical basins of the Atlantic Ocean describe the wind-driven gyre circulation, with stronger 705 poleward western boundary currents compensated by equatorward flow in the ocean interior and weaker eastern boundary currents occupying a larger longitudinal extension (**Figure 2**). Near 61 Sv of upper waters from surface, thermocline and

intermediate layers enter the Atlantic basin from the Southern and Indian Oceans at the southern boundary of our study area. The cold and fresh water route of the MC (37.2 ± 2.0 Sv) carries more water than the eastern warm and salty water route connecting the Atlantic with the Indian Ocean (24.0 ± 2.3 Sv). However, the flow of the MC retroflects and joins again the

710 ACC east of 20ºW together with a contribution from the South Atlantic subtropical gyre (-55.5 ± 5.6 Sv). The input from the Indian Ocean is divided into two nearly steady branches at 30°S, the SEC (15.8 ± 3.4 Sv on average for the whole period) and the BeC (12.5 ± 2.0 Sv on average for the whole period). Mass transports for both currents decrease on their way northward to 19°S, lowering to 2.3 ± 1.2 Sv and 9.0 ± 1.9 Sv, respectively. The complex system of currents of the South Atlantic subtropical gyre is oversimplified in **Figure 2**. All together suggests not only a northward flow of the BeC and SEC,

715 but also a large east-to-west contribution towards the BrC (ca. 2 to 7 Sv) between 24°S and 30°S. In this location a widening of the SEC is also observed (**Figure 2**). In the solutions for the cruises obtained during the 2000-2009 decade, this east-to-west contribution seems to be feeding the southward transport of the BrC at 30°S, while the circulation is harder to infer for the other periods. The 11°S section marks the end of the South Atlantic subtropical gyre where the NBrC transports northward 17.0 ± 1.2 Sv. Nearly half of the transport of this current finds its source on the northwestward SEC (9.0 ± 1.9

720 Sv).

In the northern hemisphere, both the FC and the AC carry northward warm waters from the equatorial area. These currents have decreased their transport ca. 4 Sv in the last estimate. The GF transport increases by 29.6 ± 1.8 Sv from 24ºN to 36ºN (**Figure 2**). At 36ºN, the GS carries 74.9 ± 1.7 Sv, of which -35.4 ± 3.0 Sv recirculates southward. The GS at this latitude feeds both the North Atlantic subtropical and subpolar gyres. A nearly steady transport of 5.3 ± 1.8 Sv (average transport for

725 the three decades) recirculates southward on the CC closing the subtropical loop. Between 24°N and 55°N, there is a sink to deeper layers of over 5 Sv, with the remaining transport flowing northward on the NAC contributing to the SPNA (Caínzos et al., 2022). Part of this flow enters on the Arctic basin through the Iceland-Scotland Ridge, of which about 2 Sv recirculates through the gyre and a roughly average of 5.3 ± 3.5 Sv contributes to the NIIC. The EGC connects the Arctic Basin surface waters with those within the SPNA. Interestingly, both the EGC and its downstream continuations on the Labrador Sea

730 (uWGC and LC) show increasing transports that double from the first to the last cruise. This behaviour supports the observations of an "Atlantification" of the Arctic Basin (Polyakov et al., 2020, 2017). The low values found for the ERRC and EGC transports as well as the overestimations of the ISOW can be explained by the inability of the inverse model to reproduce currents with a strong barotropic component.

The southward flow in deep layers enters the Atlantic basin at the northernmost section via the ISOW and DSOW (**Figure**

735 **2**). The stable ISOW (10.1 ± 8.9 Sv on average) carries southward relatively more water than the combined pathways of the DSOW (8.6 ± 11.3, 7.9 ± 1.05 and 7.1 ± 6.7 Sv). The net DSOW manifest decreasing values, but the large uncertainties mask any possible significant trend. Deep currents in the Labrador basin flow cyclonically, with a null net transport out of the Labrador Sea for the first decade and over 2.5 Sv for the 2000-09 and 2010-19 decades.

On its way south, deep layers show the continuity of the DWBC Current throughout the basin (**Figure 2**). At 47°N, the

740 DWBC conveys an average transport of 33.8 ± 11.9 Sv southward after turning westward at Flemish Cap (**Figure 1**). The

DWBC maintains similar strength at 36°N and then reduces at 24°N, where different values appear for each decade. There is a reduction in the estimation for the cruise obtained in 2000-09, followed by a recovery in the last cruise included in the 2010-19 period. The DWBC reaches 11°S carrying -17.3 ± 2.2 Sv southward, increasing by 17% its transport as it approaches 19°S. South of this latitude, the DWBC separates into a western branch flowing along the western boundary and an eastern branch that crosses the MAR towards the eastern basin (**Figure 2**). At 24°S, the DWBC has increased to an average value of -28.3 ± 11.4 Sv, similar to the mean transport at 30°S (-26.8 ± 7.4 Sv) This increase could be associated to an upward vertical flux from abyssal to deep layers between 24°S and 24°N for the cruises included in the 2000-09 and 2010-19 decades of 0.8 and 1.9 Sv, respectively. The export of deep transport through the western basin at 45°S rises by almost 50% to -49.1 ± 7.0 Sv. The eastern branch, the DEBC, suffers a reduction in its strength on its way south. From a mean value of -11.7 ± 8.2 Sv at 24ºS, the DEBC is reduced to -8.9 ± 7.5 Sv at 30ºS by 24%. The net export at 45°S via the eastern basin results in -6.4 ± 6.3 Sv (after a 28% reduction), corresponding to a 12% of the total deep outflow at the southern boundary of the Atlantic.

Abyssal layers are mainly confined to the South Atlantic, with a stronger net northward input via the western basin (**Figure 2**). East of the MAR, the northward transport of AABW is recirculated, describing a clockwise gyre in abyssal layers up to 24°S. On the western basin, the AABW flows northward, from 4.7 ± 1.5 Sv at 45°S to a mean value of 3.6 ± 2.4 Sv at 30°S, decreasing by 23%. West of the MAR at 24°S, the AABW exhibits different values in different decades with a significant reduction compared to the estimates at 30°S. The northward mass transport of 1.2 ± 1.2 Sv at 11°S reaches 24°N with almost negligible values (0.4 ± 1.8 Sv on average). AABW is not detected north of 24°N. We found no significant changes in transport. However, we can observe a warming trend with time in the TWT, not accompanied by freshening of the abyssal waters. Recent publications have found evidence of this increase in AABW temperature with steady and significant rates around 0.02°C decade^{-1} using different datasets and periods of time (Chidichimo et al., 2023; Johnson et al., 2020; Meinen et al., 2020; Campos et al., 2021; Zenk and Morozov, 2007; Herrford et al., 2017).

The heat transport introduced in the South Atlantic by the warm and salty water route of the Agulhas leakage is 1.19 ± 0.11 PW, distributed along the eastern basin. This heat transport is divided into the contributions for the BeC and SEC, both reducing its heat transport northward (**Figure 3**). The cold and fresh water route, instead, only transports, 0.54 ± 0.02 PW northward, with a southward heat transport toward the Southern Ocean via ACC of -1.09 ± 0.07 PW. The BrC carries heat between 19°S and 30°S along the western boundary, with higher values at 30ºS. As a result, the South Atlantic exports roughly 1 PW to the northern hemisphere carried by the NBrC. The northward transport of heat in upper layers of the North Atlantic is mainly achieved by the strong heat transported by the FC (2.48 ± 0.03 PW on average) that increases to 4.56 ± 0.11 PW in the GS at 36°N. The convection processes in the SPNA result in a decrease of heat transport to 1.79 ± 0.14 and 1.18 ± 0.05 PW for the NAC at 47°N. In deep layers, the DWBC carries roughly -0.3 PW southward, starting at 47°N from the Grand banks throughout the North Atlantic and the South Atlantic up to 24°S (**Figure 3**). The DWBC continues carrying around -0.3 PW southward along the western boundary until 45°S, where the net transport of heat via deep layers increases to -0.53 ± 0.07 PW due to the strong values of the MC. At 24°S, the DEBC carries almost half of the estimate for the

775   DWBC, introducing an average of -0.13 ± 0.08 PW into the eastern subbasin. This heat transport reduces southward, with a net export at the southernmost boundary of -0.06 ± 0.06 PW.

The freshwater flux is confined to upper layers (**Figure 4**), with a transport into the South Atlantic via the MC of 0.07 ± 0.01 Sv, counteracted by the -0.07 ± 0.02 Sv of the BeC. However, the ACC exports double of these values towards the Southern Ocean. The BrC carries freshwater northward, while the BeC shows, northward of 45°S, non-significant values of freshwater

780   flux along the eastern boundary. In the South Atlantic, the overturning component of the freshwater flux (the baroclinic transport due to the zonally averaged vertical-meridional circulation) has been identified as a possible indicator of the stability of the AMOC (Dijkstra, 2007; Weijer et al., 2019; Rahmstorf, 1996). Assessing and monitoring the freshwater budget in the South Atlantic is an important tool in determining whether the Atlantic Ocean behaves with a monostable or bistable regime. The negative or positive sign of this overturning freshwater flux (either due to a southward or northward

785   transport of freshwater in the southern boundary of the Atlantic Ocean, respectively) informs of the net precipitation or evaporation (respectively) over the basin.

In the North Atlantic, there is mainly a southward freshwater flux along the eastern basin. In general, we cannot find any pattern of change of strength of the currents with time, with similar estimations obtained for the different decades. No changes in TW properties have been observed either.

790   **Acknowledgments**

This study was supported by the SAGA project (RTI2018-100844-B-C31) funded by the Ministerio de Ciencia, Innovación y Universidades of the Spanish Government. This article is a publication of the Unidad Océano y Clima from the Universidad de Las Palmas de Gran Canaria, a R&D&I CSIC-associate unit. We thank the chief scientists and teams that collected all the data for the zonal sections: P. Saunders, T. Müller, G. Siedler, G. Parrilla, A. Sy, J. Lazier, M. Bersch, Y.

795   Yoshikawa, B. King, S. Cunningham, G. Harrison, G.-J. Brummer, M. Baringer, A. Macdonald, D. Kieke and P. Holliday. This work has been completed as part of V.C. work at IOCAG, in the doctoral program in Oceanography and Global Change. V.C. and C. A.-P. acknowledge the Agencia Canaria de Investigación, Innovación y Sociedad de la Información (ACIISI) grant program of "Apoyo al personal investigador en formación" TESIS2019010015 and TESIS2021010028, respectively. D. S.-T. acknowledges the Ministerio de Universidades grant program of "Formación de Profesorado

800   Universitario" FPU20/02211.

Data Availability Statement

Hydrographic data were collected from the CCHDO website (https://cchdo.ucsd.edu) in the frame of International WOCE and GO-SHIP projects. The Florida Current cable and section data are made freely available on the Atlantic Oceanographic and Meteorological Laboratory web page (www.aoml.noaa.gov/phod/floridacurrent/) and are funded by the DOC-NOAA

805   Climate Program Office - Ocean Observing and Monitoring Division. Florida Current daily mean transport from year 2000 until present is available at https://www.aoml.noaa.gov/phod/floridacurrent/data_access.php and historical data from 1982 to 1998 at https://www.aoml.noaa.gov/phod/floridacurrent/historical_data.php, of which we have used the used data from 1990 to 1998. The daily mean u and v-wind components of NCEP/NCAR reanalysis winds were collected from https://psl.noaa.gov/data/gridded/data.ncep.reanalysis.pressure.html. Results from the inverse solutions can be provided upon

810   request.

References

Álvarez, M., Bryden, H. L., Pérez, F. F., Ríos, A. F., and Rosón, G.: Physical and biogeochemical fluxes and net budgets in the subpolar and temperate North Atlantic, J Mar Res, 60, 191–226, 2002.

815   Arhan, M., Mercier, H., and Park, Y. H.: On the deep water circulation of the eastern South Atlantic Ocean, Deep Sea Res 1 Oceanogr Res Pap, 50, 889–916, https://doi.org/10.1016/S0967-0637(03)00072-4, 2003.

Artana, C., Ferrari, R., Koenig, Z., Sennéchael, N., Saraceno, M., Piola, A. R., and Provost, C.: Malvinas current volume transport at 41°S: A 24 yearlong time series consistent with mooring data from 3 decades and satellite altimetry, J Geophys Res Oceans, 123, 378–398, https://doi.org/10.1002/2017JC013600, 2018.

820   Arumí-Planas, C., Pérez-Hernández, M. D., Pelegrí, J. L., Vélez-Belchí, P., Emelianov, M., Caínzos, V., Cana, L., Firing, Y. L., García-Weil, L., Santana-Toscano, D., and Hernández-Guerra, A.: The South Atlantic Circulation Between 34.5°S, 24°S and Above the Mid-Atlantic Ridge From an Inverse Box Model, J Geophys Res Oceans, 128, 1–21, https://doi.org/10.1029/2022JC019614, 2023.

Atkinson, C. P., Bryden, H. L., Hirschi, J. J. M., and Kanzow, T.: On the seasonal cycles and variability of Florida Straits, 825   Ekman and Sverdrup transports at 26°N in the Atlantic Ocean, Ocean Science, 6, 837–859, https://doi.org/10.5194/os-6-837-2010, 2010.

Bacon, S.: Circulation and fluxes in the North Atlantic between Greenland and Ireland, J Phys Oceanogr, 27, 1420–1435, https://doi.org/10.1175/1520-0485(1997)027<1420:cafitn>2.0.co;2, 1997.

Baringer, M. O. N. and Larsen, J. C.: Sixteen years of Florida Current Transport at 27° N, Geophys Res Lett, 28, 3179–3182, 830   https://doi.org/10.1029/2001GL013246, 2001.

Bersch, M., Yashayaev, I., and Koltermann, K. P.: Recent changes of the thermohaline circulation in the subpolar North Atlantic, Ocean Dyn, 57, 223–235, https://doi.org/10.1007/s10236-007-0104-7, 2007.

Biló, T. C. and Johns, W. E.: The Deep Western Boundary Current and Adjacent Interior Circulation at 24°–30°N: Mean Structure and Mesoscale Variability, J Phys Oceanogr, 50, 2735–2758, https://doi.org/10.1175/JPO-D-20-0094.1, 2020.

835   Boebel, O., Davis, R. E., Ollitrault, M., Peterson, R. G., Richardson, P. L., Schmid, C., and Zenk, W.: The intermediate depth circulation of the western South Atlantic, Geophys Res Lett, 26, 3329–3332, https://doi.org/10.1029/1999GL002355, 1999.

Bower, A., Lozier, S., Biastoch, A., Drouin, K., Foukal, N., Furey, H., Lankhorst, M., Rühs, S., and Zou, S.: Lagrangian Views of the Pathways of the Atlantic Meridional Overturning Circulation, J Geophys Res Oceans, 124, 5313–5335,

840   https://doi.org/10.1029/2019JC015014, 2019.

le Bras, I. A., Straneo, F., Holte, J., and Holliday, N. P.: Seasonality of Freshwater in the East Greenland Current System From 2014 to 2016, J Geophys Res Oceans, 123, 8828–8848, https://doi.org/10.1029/2018JC014511, 2018.

Brearley, J. A., Pickart, R. S., Valdimarsson, H., Jonsson, S., Schmitt, R. W., and Haine, T. W. N.: The East Greenland boundary current system south of Denmark Strait, Deep Sea Research Part I: Oceanographic Research Papers, 63, 1–19,

845   https://doi.org/10.1016/j.dsr.2012.01.001, 2012.

Bryden, H. L., Johns, W. E., and Saunders, P. M.: Deep western boundary current east of Abaco: Mean structure and transport, J Mar Res, 63, 35–57, https://doi.org/10.1357/0022240053693806, 2005a.

Bryden, H. L., Longworth, H. R., and Cunningham, S. A.: Slowing of the Atlantic meridional overturning circulation at 25° N, Nature, 438, 655–657, https://doi.org/10.1038/nature04385, 2005b.

850   Bryden, H. L., King, B. A., and McCarthy, G. D.: South Atlantic overturning circulation at 24°S, J Mar Res, 69, 39–56, https://doi.org/10.1357/002224011798147633, 2011.

Caínzos, V., Hernández-Guerra, A., McCarthy, G. D., McDonagh, E. L., Cubas Armas, M., and Pérez-Hernández, M. D.: Thirty Years of GOSHIP and WOCE Data: Atlantic Overturning of Mass, Heat, and Freshwater Transport, Geophys Res Lett, 49, https://doi.org/10.1029/2021GL096527, 2022.

855   Campos, E. J. D., van Caspel, M. C., Zenk, W., Morozov, E. G., Frey, D. I., Piola, A. R., Meinen, C. S., Sato, O. T., Perez, R. C., and Dong, S.: Warming Trend in Antarctic Bottom Water in the Vema Channel in the South Atlantic, Geophys Res Lett, 48, 1–7, https://doi.org/10.1029/2021GL094709, 2021.

Casanova-Masjoan, M., Joyce, T. M., Pérez-Hernández, M. D., Vélez-Belchí, P., and Hernández-Guerra, A.: Changes across 66°W, the Caribbean Sea and the Western boundaries of the North Atlantic Subtropical Gyre, Prog Oceanogr, 168, 296–309,

860   https://doi.org/10.1016/j.pocean.2018.09.013, 2018.

Casanova-Masjoan, M., Pérez-Hernández, M. D., Pickart, R. S., Valdimarsson, H., Ólafsdóttir, S. R., Macrander, A., Grisolía-Santos, D., Torres, D. J., Jónsson, S., Våge, K., Lin, P., and Hernández-Guerra, A.: Along-Stream, Seasonal, and Interannual Variability of the North Icelandic Irminger Current and East Icelandic Current Around Iceland, J Geophys Res Oceans, 125, 1–24, https://doi.org/10.1029/2020JC016283, 2020.

865   Casanova-Masjoan, M., Pérez-Hernández, M. D., Vélez-Belchí, P., Cana, L., and Hernández-Guerra, A.: Variability of the Canary Current diagnosed by inverse box models, J Geophys Res Oceans, 125, e2020JC016199, https://doi.org/10.1029/2020JC016199, 2020.

Chidichimo, M. P., Perez, R. C., Speich, S., Kersalé, M., Sprintall, J., Dong, S., Lamont, T., Sato, O. T., Chereskin, T. K., Hummels, R., and Schmid, C.: Energetic overturning flows, dynamic interocean exchanges, and ocean warming observed in

870   the South Atlantic, Commun Earth Environ, 4, 10, https://doi.org/10.1038/s43247-022-00644-x, 2023.

Comas-Rodríguez, I., Hernández-Guerra, A., Fraile-Nuez, E., Martínez-Marrero, A., Benítez-Barrios, V. M., Pérez-Hernández, M. D., and Vélez-Belchí, P.: The Azores Current System from a meridional section at 24.5°W, J Geophys Res, 116, C09021, https://doi.org/10.1029/2011JC007129, 2011.

Cunningham, S. A., Kanzow, T., Rayner, D., Baringer, M. O., Johns, W. E., Marotzke, J., Longworth, H. R., Grant, E. M.,

875   Hirschi, J. J. M., Beal, L. M., Meinen, C. S., and Bryden, H. L.: Temporal variability of the Atlantic meridional overturning circulation at 26.5°N, Science (1979), 317, 935–938, https://doi.org/10.1126/science.1141304, 2007.

Daniault, N., Mercier, H., Lherminier, P., Sarafanov, A., Falina, A., Zunino, P., Pérez, F. F., Ríos, A. F., Ferron, B., Huck, T., Thierry, V., and Gladyshev, S.: The northern North Atlantic Ocean mean circulation in the early 21st century, Prog Oceanogr, 146, 142–158, https://doi.org/10.1016/j.pocean.2016.06.007, 2016.

880   Davis, R. E., Regier, L. A., Dufour, J., and Webb, D. C.: The Autonomous Lagrangian Circulation Explorer (ALACE), J Atmos Ocean Technol, 9, 264–285, https://doi.org/10.1175/1520-0426(1992)009<0264:TALCE>2.0.CO;2, 1992.

Dickson, B., Dye, S., Jónsson, S., Köhl, A., Macrander, A., Marnela, M., Meincke, J., Olsen, S., Rudels, B., Valdimarsson, H., and Voet, G.: The Overflow Flux West of Iceland: Variability, Origins and Forcing, in: Arctic–Subarctic Ocean Fluxes, Springer Netherlands, Dordrecht, 443–474, https://doi.org/10.1007/978-1-4020-6774-7_20, 2008.

885   Dijkstra, H. A.: Characterization of the multiple equilibria regime in a global ocean model, Tellus, 59A, 695–705, https://doi.org/10.1111/j.1600-0870.2007.00267.x, 2007.

Durgadoo, J. v., Rühs, S., Biastoch, A., and Böning, C. W. B.: Indian Ocean sources of Agulhas leakage, J Geophys Res Oceans, 122, 3481–3499, https://doi.org/10.1002/2016JC012676, 2017.

Evans, G. R., McDonagh, E. L., King, B. A., Bryden, H. L., Bakker, D. C. E., Brown, P. J., Schuster, U., Speer, K. G., and

890   Heuven, S. M. A. C. van: South Atlantic interbasin exchanges of mass, heat, salt and anthropogenic carbon, Prog Oceanogr, 151, 62–82, https://doi.org/10.1016/j.pocean.2016.11.005, 2017.

Fischer, J., Schott, F. A., and Dengler, M.: Boundary Circulation at the Exit of the Labrador Sea, J Phys Oceanogr, 34, 1548–1570, https://doi.org/10.1175/1520-0485(2004)034<1548:BCATEO>2.0.CO;2, 2004.

Fischer, J., Visbeck, M., Zantopp, R., and Nunes, N.: Interannual to decadal variability of outflow from the Labrador Sea,

895   Geophys Res Lett, 37, https://doi.org/10.1029/2010GL045321, 2010.

Fischer, J., Karstensen, J., Zantopp, R., Visbeck, M., Biastoch, A., Behrens, E., Böning, C. W., Quadfasel, D., Jochumsen, K., Valdimarsson, H., Jónsson, S., Bacon, S., Holliday, N. P., Dye, S., Rhein, M., and Mertens, C.: Intra-seasonal variability of the DWBC in the western subpolar North Atlantic, Prog Oceanogr, 132, 233–249, https://doi.org/10.1016/j.pocean.2014.04.002, 2015.

900 Florindo-López, C., Bacon, S., Aksenov, Y., Chafik, L., Colbourne, E., and Holliday, N. P.: Arctic Ocean and Hudson Bay freshwater exports: new estimates from seven decades of hydrographic surveys on the Labrador Shelf, J Clim, 33, 8849–8868, https://doi.org/10.1175/JCLI-D-19-0083.1, 2020.

Foppert, A., Rintoul, S. R., Purkey, S. G., Zilberman, N., Kobayashi, T., Sallèe, J., Wijk, E. M., and Wallace, L. O.: Deep Argo Reveals Bottom Water Properties and Pathways in the Australian-Antarctic Basin, J Geophys Res Oceans, 126, 1–18,
905 https://doi.org/10.1029/2021JC017935, 2021.

Forget, G. and Ferreira, D.: Global ocean heat transport dominated by heat export from the tropical Pacific, Nat Geosci, 12, 351–354, https://doi.org/10.1038/s41561-019-0333-7, 2019.

Fraile-Nuez, E., Machín, F., Vélez-Belchí, P., López-Laatzen, F., Borges, R., Benítez-Barrios, V. M., and Hernández-Guerra, A.: Nine years of mass transport data in the eastern boundary of the North Atlantic Subtropical Gyre, J Geophys Res,
910 115, C09009, https://doi.org/10.1029/2010JC006161, 2010.

Frajka-Williams, E., Cunningham, S. A., Bryden, H. L., and King, B. A.: Variability of Antarctic Bottom Water at 24.5°N in the Atlantic, J Geophys Res, 116, C11026, https://doi.org/10.1029/2011JC007168, 2011.

Frajka-Williams, E., Ansorge, I. J., Baehr, J., Bryden, H. L., Chidichimo, M. P., Cunningham, S. A., Danabasoglu, G., Dong, S., Donohue, K. A., Elipot, S., Heimbach, P., Holliday, N. P., Hummels, R., Jackson, L. C., Karstensen, J., Lankhorst, M.,
915 Le Bras, I. A., Lozier, M. S., McDonagh, E. L., Meinen, C. S., Mercier, H., Moat, B. I., Perez, R. C., Piecuch, C. G., Rhein, M., Srokosz, M. A., Trenberth, K. E., Bacon, S., Forget, G., Goni, G., Kieke, D., Koelling, J., Lamont, T., McCarthy, G. D., Mertens, C., Send, U., Smeed, D. A., Speich, S., van den Berg, M., Volkov, D., and Wilson, C.: Atlantic Meridional Overturning Circulation: Observed Transport and Variability, Front Mar Sci, 6, https://doi.org/10.3389/fmars.2019.00260, 2019.

920 Frankignoul, C., de Coëtlogon, G., Joyce, T. M., and Dong, S.: Gulf Stream Variability and Ocean–Atmosphere Interactions, J Phys Oceanogr, 31, 3516–3529, https://doi.org/10.1175/1520-0485(2002)031<3516:GSVAOA>2.0.CO;2, 2001.

Fu, Y., Li, F., Karstensen, J., and Wang, C.: A stable Atlantic Meridional Overturning Circulation in a changing North Atlantic Ocean since the 1990s, Sci Adv, 6, eabc7836, https://doi.org/10.1126/sciadv.abc7836, 2020.

Ganachaud, A. S.: Error budget of inverse box models: The North Atlantic, J Atmos Ocean Technol, 20, 1641–1655,
925 https://doi.org/10.1175/1520-0426(2003)020<1641:EBOIBM>2.0.CO;2, 2003a.

Ganachaud, A. S.: Large-scale mass transports, water mass formation, and diffusivities estimated from World Ocean Circulation Experiment (WOCE) hydrographic data, J Geophys Res, 108, https://doi.org/10.1029/2002jc001565, 2003b.

Ganachaud, A. S. and Wunsch, C.: Improved estimates of global ocean circulation, heat transport and mixing from hydrographic data, Nature, 408, 453–456, 2000.

930 Ganachaud, A. S. and Wunsch, C.: Large-scale ocean heat and freshwater transports during the World Ocean Circulation Experiment, J Clim, 16, 696–705, https://doi.org/10.1175/1520-0442(2003)016<0696:LSOHAF>2.0.CO;2, 2003.

García-Ibáñez, M. I., Pardo, P. C., Carracedo, L. I., Mercier, H., Lherminier, P., Ríos, A. F., and Pérez, F. F.: Structure, transports and transformations of the water masses in the Atlantic Subpolar Gyre, Prog Oceanogr, 135, 18–36, https://doi.org/10.1016/j.pocean.2015.03.009, 2015.

935 Garzoli, S. L.: Geostrophic velocity and transport variability in the Brazil-Malvinas Confluence, Deep Sea Research Part I: Oceanographic Research Papers, 40, 1379–1403, https://doi.org/10.1016/0967-0637(93)90118-M, 1993.

Garzoli, S. L.: North Brazil Current retroflection and transports, J Geophys Res, 109, C01013, https://doi.org/10.1029/2003JC001775, 2004.

Garzoli, S. L. and Gordon, A. L.: Origins and variability of the Benguela Current, J Geophys Res Oceans, 101, 897–906,
940 https://doi.org/10.1029/95JC03221, 1996.

Garzoli, S. L., Gordon, A. L., Kamenkovich, V., Pillsbury, D., and Duncombe-Rae, C.: Variability and sources of the southeastern Atlantic circulation, J Mar Res, 54, 1039–1071, https://doi.org/10.1357/0022240963213763, 1996.

Garzoli, S. L., Baringer, M. O., Dong, S., Perez, R. C., and Yao, Q.: South Atlantic meridional fluxes, Deep Sea Res 1 Oceanogr Res Pap, 71, 21–32, https://doi.org/10.1016/j.dsr.2012.09.003, 2013.

945 Garzoli, S. L., Dong, S., Fine, R., Meinen, C. S., Perez, R. C., Schmid, C., van Sebille, E., and Yao, Q.: The fate of the Deep Western Boundary Current in the South Atlantic, Deep Sea Research Part I: Oceanographic Research Papers, 103, 125–136, https://doi.org/10.1016/j.dsr.2015.05.008, 2015.

Goni, G., Kamholz, S., Garzoli, S., and Olson, D.: Dynamics of the Brazil-Malvinas Confluence based on inverted echo sounders and altimetry, J Geophys Res Oceans, 101, 16273–16289, https://doi.org/10.1029/96JC01146, 1996.

950 Gou, R., Pennelly, C., and Myers, P. G.: The Changing Behavior of the West Greenland Current System in a Very High-Resolution Model, J Geophys Res Oceans, 127, 1–15, https://doi.org/10.1029/2022JC018404, 2022.

Harden, B. E., Pickart, R. S., Valdimarsson, H., Våge, K., de Steur, L., Richards, C., Bahr, F., Torres, D., Børve, E., Jónsson, S., Macrander, A., Østerhus, S., Håvik, L., and Hattermann, T.: Upstream sources of the Denmark Strait Overflow: Observations from a high-resolution mooring array, Deep Sea Research Part I: Oceanographic Research Papers, 112, 94–
955 112, https://doi.org/10.1016/j.dsr.2016.02.007, 2016.

Hernández-Guerra, A. and Talley, L. D.: Meridional overturning transports at 30°S in the Indian and Pacific Oceans in 2002–2003 and 2009, Prog Oceanogr, 146, 89–120, https://doi.org/10.1016/j.pocean.2016.06.005, 2016.

Hernández-Guerra, A., Pelegrí, J. L., Fraile-Nuez, E., Benítez-Barrios, V. M., Emelianov, M., Pérez-Hernández, M. D., and Vélez-Belchí, P.: Meridional overturning transports at 7.5N and 24.5N in the Atlantic Ocean during 1992–93 and 2010–11,
960 Prog Oceanogr, 128, 98–114, https://doi.org/10.1016/j.pocean.2014.08.016, 2014.

Hernández-Guerra, A., Espino-Falcón, E., Vélez-Belchí, P., Dolores Pérez-Hernández, M., Martínez-Marrero, A., and Cana, L.: Recirculation of the Canary Current in fall 2014, Journal of Marine Systems, 174, 25–39, https://doi.org/10.1016/j.jmarsys.2017.04.002, 2017.

Hernández-Guerra, A., Talley, L. D., Pelegrí, J. L., Vélez-Belchí, P., Baringer, M. O., Macdonald, A. M., and McDonagh, E.
L.: The upper, deep, abyssal and overturning circulation in the Atlantic Ocean at 30°S in 2003 and 2011, Prog Oceanogr, 176, https://doi.org/10.1016/j.pocean.2019.102136, 2019.

Herrford, J., Brandt, P., and Zenk, W.: Property changes of deep and bottom waters in the Western Tropical Atlantic, Deep Sea Research Part I: Oceanographic Research Papers, 124, 103–125, https://doi.org/10.1016/j.dsr.2017.04.007, 2017.

Hogg, N. G.; and Johns, W. E.: Western boundary currents, Reviews of Geophysics, 33, 1311–1334, https://doi.org/10.1029/95RG00491, 1995.

Holliday, N. P., Bacon, S., Cunningham, S. A., Gary, S. F., Karstensen, J., King, B. A., Li, F., and Mcdonagh, E. L.: Subpolar North Atlantic Overturning and Gyre-Scale Circulation in the Summers of 2014 and 2016, J Geophys Res Oceans, 123, 4538–4559, https://doi.org/10.1029/2018JC013841, 2018.

Houpert, L., Inall, M. E., Dumont, E., Gary, S., Johnson, C., Porter, M., Johns, W. E., and Cunningham, S. A.: Structure and transport of the North Atlantic Current in the Eastern Subpolar Gyre from sustained glider observations, J Geophys Res Oceans, 123, 6019–6038, https://doi.org/10.1029/2018JC014162, 2018.

Hummels, R., Brandt, P., Dengler, M., Fischer, J., Araujo, M., Veleda, D., and Durgadoo, J. v.: Interannual to decadal changes in the western boundary circulation in the Atlantic at 11°S, Geophys Res Lett, 42, 7615–7622, https://doi.org/10.1002/2015GL065254, 2015.

Jayne, S. R. and Marotzke, J.: The dynamics of ocean heat transport variability, Reviews of Geophysics, 39, 385–411, https://doi.org/10.1029/2000RG000084, 2001.

Jochumsen, K., Quadfasel, D., Valdimarsson, H., and Jónsson, S.: Variability of the Denmark Strait overflow: Moored time series from 1996-2011, J Geophys Res Oceans, 117, https://doi.org/10.1029/2012JC008244, 2012.

Johns, W. E., Shay, T. J., Bane, J. M., and Watts, D. R.: Gulf Stream structure, transport, and recirculation near 68°W, J Geophys Res, 100, 817, https://doi.org/10.1029/94JC02497, 1995.

Johns, W. E., Beal, L. M., Baringer, M. O., Molina, J. R., Cunningham, S. A., Kanzow, T., and Rayner, D.: Variability of Shallow and Deep Western Boundary Currents off the Bahamas during 2004–05: Results from the 26°N RAPID–MOC Array, J Phys Oceanogr, 38, 605–623, https://doi.org/10.1175/2007jpo3791.1, 2008.

Johns, W. E., Baringer, M. O., Beal, L. M., Cunningham, S. A., Kanzow, T., Bryden, H. L., Hirschi, J. J. M., Marotzke, J., Meinen, C. S., Shaw, B., and Curry, R.: Continuous, array-based estimates of Atlantic Ocean heat transport at 26.5°N, J Clim, 24, 2429–2449, https://doi.org/10.1175/2010JCLI3997.1, 2011.

Johns, W. E., Devana, M., Houk, A., and Zou, S.: Moored Observations of the Iceland-Scotland Overflow Plume Along the Eastern Flank of the Reykjanes Ridge, J Geophys Res Oceans, 126, 1–26, https://doi.org/10.1029/2021JC017524, 2021.

Johnson, G. C., Lyman, J. M., and Purkey, S. G.: Informing Deep Argo Array Design Using Argo and Full-Depth Hydrographic Section Data, J Atmos Ocean Technol, 32, 2187–2198, https://doi.org/10.1175/JTECH-D-15-0139.1, 2015.

Johnson, G. C., Purkey, S. G., Zilberman, N. v., and Roemmich, D.: Deep Argo Quantifies Bottom Water Warming Rates in the Southwest Pacific Basin, Geophys Res Lett, 46, 2662–2669, https://doi.org/10.1029/2018GL081685, 2019.

Johnson, G. C., Cadot, C., Lyman, J. M., McTaggart, K. E., and Steffen, E. L.: Antarctic Bottom Water Warming in the Brazil Basin: 1990s Through 2020, From WOCE to Deep Argo, Geophys Res Lett, 47, https://doi.org/10.1029/2020GL089191, 2020.

Kanzow, T., Send, U., Zenk, W., Chave, A. D., and Rhein, M.: Monitoring the integrated deep meridional flow in the tropical North Atlantic: Long-term performance of a geostrophic array, Deep Sea Res 1 Oceanogr Res Pap, 53, 528–546, https://doi.org/10.1016/j.dsr.2005.12.007, 2006.

Katsumata, K. and Fukasawa, M.: Changes in meridional fluxes and water properties in the Southern Hemisphere subtropical oceans between 1992/1995 and 2003/2004, Prog Oceanogr, 89, 61–91, https://doi.org/10.1016/j.pocean.2010.12.008, 2011.

Kersalé, M., Perez, R. C., Speich, S., Meinen, C. S., Lamont, T., le Hénaff, M., van den Berg, M. A., Majumder, S., Ansorge, I. J., Dong, S., Schmid, C., Terre, T., and Garzoli, S. L.: Shallow and Deep Eastern Boundary Currents in the South Atlantic at 34.5°S: Mean Structure and Variability, J Geophys Res Oceans, 124, 1634–1659, https://doi.org/10.1029/2018JC014554, 2019.

Kersalé, M., Meinen, C. S., Perez, R. C., le Hénaff, M., Valla, D., Lamont, T., Sato, O. T., Dong, S., Terre, T., van Caspel, M., Chidichimo, M. P., van den Berg, M., Speich, S., Piola, A. R., Campos, E. J. D., Ansorge, I., Volkov, D. L., Lumpkin, R., and Garzoli, S. L.: Highly variable upper and abyssal overturning cells in the South Atlantic, Sci Adv, 6, eaba7573, https://doi.org/10.1126/sciadv.aba7573, 2020.

King, B. A., Sanchez-Franks, A., and Firing, Y. L.: RRS James Cook Cruise JC159 28 February - 11 April 2018. Hydrographic sections from the Brazil to the Benguela Current across 24S in the Atlantic, National Oceanography Centre Cruise Report, Southampton, UK, 193 pp., 2019.

Koltermann, K. P., Sokov, A. v., Tereschenkov, V. P., Dobroliubov, S. A., Lorbacher, K., and Sy, A.: Decadal changes in the thermohaline circulation of the North Atlantic, Deep Sea Res 2 Top Stud Oceanogr, 46, 109–138, https://doi.org/10.1016/S0967-0645(98)00115-5, 1999.

Koszalka, I. M., Haine, T. W. N., and Magaldi, M. G.: Fates and Travel Times of Denmark Strait Overflow Water in the Irminger Basin*, J Phys Oceanogr, 43, 2611–2628, https://doi.org/10.1175/JPO-D-13-023.1, 2013.

Lazier, J., Hendry, R., Clarke, A., Yashayaev, I., and Rhines, P.: Convection and restratification in the Labrador Sea, 1990–2000, Deep Sea Research Part I: Oceanographic Research Papers, 49, 1819–1835, https://doi.org/10.1016/S0967-0637(02)00064-X, 2002.

Lee, T. N., Johns, W. E., Zantopp, R. J., and Fillenbaum, E. R.: Moored Observations of Western Boundary Current Variability and Thermohaline Circulation at 26.5° in the Subtropical North Atlantic, J Phys Oceanogr, 26, 962–983, https://doi.org/10.1175/1520-0485(1996)026<0962:MOOWBC>2.0.CO;2, 1996.

Legeais, J.-F., Ollitrault, M., and Arhan, M.: Lagrangian observations in the Intermediate Western Boundary Current of the South Atlantic, Deep Sea Research Part II: Topical Studies in Oceanography, 85, 109–126, https://doi.org/10.1016/j.dsr2.2012.07.028, 2013.

Legeckis, R. and Gordon, A. L.: Satellite observations of the Brazil and Falkland currents— 1975 1976 and 1978, Deep Sea Research Part A. Oceanographic Research Papers, 29, 375–401, https://doi.org/10.1016/0198-0149(82)90101-7, 1982.

Lherminier, P., Mercier, H., Gourcuff, C., Alvarez, M., Bacon, S., and Kermabon, C.: Transports across the 2002 Greenland-Portugal Ovide section and comparison with 1997, J Geophys Res, 112, C07003, https://doi.org/10.1029/2006JC003716, 2007.

Lherminier, P., Mercier, H., Huck, T., Gourcuff, C., Pérez, F. F., Morin, P., Sarafanov, A., and Falina, A.: The Atlantic Meridional Overturning Circulation and the subpolar gyre observed at the A25-OVIDE section in June 2002 and 2004, Deep Sea Research Part I: Oceanographic Research Papers, 57, 1374–1391, https://doi.org/10.1016/j.dsr.2010.07.009, 2010.

Li, F. and Lozier, M. S.: On the linkage between Labrador Sea Water volume and overturning circulation in the Labrador Sea: A case study on proxies, J Clim, 31, 5225–5241, https://doi.org/10.1175/JCLI-D-17-0692.1, 2018.

Lozier, M. S., Bacon, S., Bower, A. S., Cunningham, S. A., de Jong, M. F., Steur, L. de, DeYoung, B., Fischer, J., Gary, S. F., Greenan, B. J. W., Heimbach, P., Holliday, N. P., Houpert, L., Inall, M. E., Johns, W. E., Johnson, H. L., Karstensen, J., Li, F., Lin, X., Mackay, N., and Zika, J. D.: Overturning in the Subpolar North Atlantic Program: A New International Ocean Observing System, Bull Am Meteorol Soc, 98, 737–752, https://doi.org/10.1175/bams-d-16-0057.1, 2017.

Lozier, M. S., Li, F., Bacon, S., Bahr, F., Bower, A. S., Cunningham, S. A., d Jong, M. F., de Steur, L., DeYoung, B., Fischer, J., Gary, S. F., Greenan, B. J. W., Holliday, N. P., Houk, A., Houpert, L., Inall, M. E., Johns, W. E., Johnson, H. L., Johnson, C., Karstensen, J., Koman, G., le Bras, I. A., Lin, X., Mackay, N., Marshall, D. P., Mercier, H., Oltmanns, M., Pickart, R. S., Ramsey, A. L., Rayner, D., Straneo, F., Thierry, V., Torres, D. J., Williams, R. G., Wilson, C., Yang, J., Yashayaev, I., and Zhao, J.: A sea change in our view of overturning in the subpolar North Atlantic, Science (1979), 363, 516–521, https://doi.org/10.1126/science.aau6592, 2019.

Lumpkin, R. and Speer, K. G.: Global Ocean Meridional Overturning, J Phys Oceanogr, 37, 2550–2562, https://doi.org/10.1175/jpo3130.1, 2007.

Maamaatuaiahutapu, K., Garçon, V., Provost, C., and Mercier, H.: Transports of the Brazil and Malvinas Currents at their confluence, J Mar Res, 56, 417–438, https://doi.org/10.1357/002224098321822366, 1998.

Macdonald, A. M. and Wunsch, C.: An estimate of global ocean circulation and heat fluxes, Nature, 382, 436–439, 1996.

Machín, F., Hernández-Guerra, A., and Pelegrí, J. L.: Mass fluxes in the Canary Basin, Prog Oceanogr, 70, 416–447, https://doi.org/10.1016/j.pocean.2006.03.019, 2006.

Maul, G. A. and Vukovich, F. M.: The Relationship between Variations in the Gulf of Mexico Loop Current and Straits of Florida Volume Transport, J Phys Oceanogr, 23, 785–796, https://doi.org/10.1175/1520-0485(1993)023<0785:TRBVIT>2.0.CO;2, 1993.

McCarthy, G. D., Smeed, D. A., Johns, W. E., Frajka-Williams, E., Moat, B. I., Rayner, D., Baringer, M. O., Meinen, C. S., Collins, J., and Bryden, H. L.: Measuring the Atlantic Meridional Overturning Circulation at 26°N, Prog Oceanogr, 130, 91–111, https://doi.org/10.1016/j.pocean.2014.10.006, 2015.

McCarthy, G. D., Brown, P. J., Flagg, C. N., Goni, G., Houpert, L., Hughes, C. W., Hummels, R., Inall, M., Jochumsen, K., Larsen, K. M. H., Lherminier, P., Meinen, C. S., Moat, B. I., Rayner, D., Rhein, M., Roessler, A., Schmid, C., and Smeed, D. A.: Sustainable Observations of the AMOC: Methodology and Technology, Reviews of Geophysics, 58, 1–34, https://doi.org/10.1029/2019RG000654, 2020.

McDonagh, E. L. and King, B. A.: Oceanic fluxes in the South Atlantic, J Phys Oceanogr, 35, 109–122, https://doi.org/10.1175/JPO-2666.1, 2005.

McDonagh, E. L., McLeod, P., King, B. A., Bryden, H. L., and Valdés, S. T.: Circulation, Heat, and Freshwater Transport at 36°N in the Atlantic, J Phys Oceanogr, 40, 2661–2678, https://doi.org/10.1175/2010JPO4176.1, 2010.

McDonagh, E. L., King, B. A., Bryden, H. L., Courtois, P., Szuts, Z., Baringer, M. O., Cunningham, S. A., Atkinson, C., and McCarthy, G.: Continuous estimate of Atlantic oceanic freshwater flux at 26.5°N, J Clim, 28, 8888–8906, 2015.

Meinen, C. S. and Watts, D. R.: Vertical structure and transport on a transect across the North Atlantic Current near 42°N: Time series and mean, J Geophys Res Oceans, 105, 21869–21891, https://doi.org/10.1029/2000JC900097, 2000.

Meinen, C. S., Garzoli, S. L., Johns, W. E., and Baringer, M. O.: Transport variability of the Deep Western Boundary Current and the Antilles Current off Abaco Island, Bahamas, Deep Sea Research Part I: Oceanographic Research Papers, 51, 1397–1415, https://doi.org/10.1016/j.dsr.2004.07.007, 2004.

Meinen, C. S., Speich, S., Perez, R. C., Dong, S., Piola, A. R., Garzoli, S. L., Baringer, M. O., Gladyshev, S., and Campos, E. J. D.: Temporal variability of the meridional overturning circulation at 34.5°S: Results from two pilot boundary arrays in the South Atlantic, J Geophys Res Oceans, 118, 6461–6478, https://doi.org/10.1002/2013JC009228, 2013.

Meinen, C. S., Johns, W. E., Moat, B. I., Smith, R. H., Johns, E. M., Rayner, D., Frajka-Williams, E., Garcia, R. F., and Garzoli, S. L.: Structure and Variability of the Antilles Current at 26.5°N, J Geophys Res Oceans, 124, 3700–3723, https://doi.org/10.1029/2018JC014836, 2019.

Meinen, C. S., Perez, R. C., Dong, S., Piola, A. R., and Campos, E.: Observed Ocean Bottom Temperature Variability at Four Sites in the Northwestern Argentine Basin: Evidence of Decadal Deep/Abyssal Warming Amidst Hourly to Interannual Variability During 2009–2019, Geophys Res Lett, 47, https://doi.org/10.1029/2020GL089093, 2020.

Myers, P. G., Kulan, N., and Ribergaard, M. H.: Irminger Water variability in the West Greenland Current, Geophys Res Lett, 34, L17601, https://doi.org/10.1029/2007GL030419, 2007.

Myers, P. G., Donnelly, C., and Ribergaard, M. H.: Structure and variability of the West Greenland Current in Summer derived from 6 repeat standard sections, Prog Oceanogr, 80, 93–112, https://doi.org/10.1016/j.pocean.2008.12.003, 2009.

Naveira Garabato, A. C., Williams, A. P., and Bacon, S.: The three-dimensional overturning circulation of the Southern Ocean during the WOCE era, Prog Oceanogr, 120, 41–78, https://doi.org/10.1016/j.pocean.2013.07.018, 2014.

Olson, D. B., Schott, F. A., Zantopp, R. J., and Leaman, K. D.: The Mean Circulation East of the Bahamas as Determined from a Recent Measurement Program and Historical XBT Data, J Phys Oceanogr, 14, 1470–1487, https://doi.org/10.1175/1520-0485(1984)014<1470:TMCEOT>2.0.CO;2, 1984.

Orsi, A. H., Whitworth, T., and Nowlin, W. D.: On the meridional extent and fronts of the Antarctic Circumpolar Current, Deep Sea Research Part I: Oceanographic Research Papers, 42, 641–673, https://doi.org/10.1016/0967-0637(95)00021-W, 1995.

1100 Pacini, A., Pickart, R. S., Bahr, F., Torres, D. J., Ramsey, A. L., Holte, J., Karstensen, J., Oltmanns, M., Straneo, F., le Bras, I. A., Moore, G. W. K., and Femke de Jong, M.: Mean Conditions and Seasonality of the West Greenland Boundary Current System near Cape Farewell, J Phys Oceanogr, 50, 2849–2871, https://doi.org/10.1175/JPO-D-20-0086.1, 2020.

Parrilla, G., Lavín, A., Bryden, H. L., García, M., and Millard, R.: Rising temperatures in the subtropical North Atlantic Ocean over the past 35 years, Nature, 369, 48–51, https://doi.org/10.1038/369048a0, 1994.

1105 Pérez-Hernández, M. D., Hernández-Guerra, A., Fraile-Nuez, E., Comas-Rodríguez, I., Benítez-Barrios, V. M., Domínguez-Yanes, J. F., Vélez-Belchí, P., and De Armas, D.: The source of the Canary current in fall 2009, J Geophys Res Oceans, 118, 2874–2891, https://doi.org/10.1002/jgrc.20227, 2013.

Pérez-Hernández, M. D., McCarthy, G. D., Vélez-Belchí, P., Smeed, D. A., Fraile-Nuez, E., and Hernández-Guerra, A.: The Canary Basin contribution to the seasonal cycle of the Atlantic Meridional Overturning Circulation at 26°N, J Geophys Res
1110 Oceans, 120, 7237–7252, https://doi.org/10.1002/2015JC010969, 2015.

Pérez-Hernández, M. D., Hernández-Guerra, A., Comas-Rodríguez, I., Benítez-Barrios, V. M., Fraile-Nuez, E., Pelegrí, J. L., and Naveira Garabato, A. C.: Differences between 1999 and 2010 across the Falkland Plateau: Fronts and water masses, Ocean Science, 13, 577–587, https://doi.org/10.5194/os-13-577-2017, 2017.

Pérez-Hernández, M. D., Hernández-Guerra, A., Cana-Cascallar, L., Arumí-Planas, C., Caínzos, V., González-Santana, A.
1115 J., Gutiérrez-Guerra, M. Á., Martínez-Marrero, A., Mosquera Giménez, Á., Presas Navarro, C., Santana-Toscano, D., and Vélez-Belchí, P.: The Seasonal Cycle of the Eastern Boundary Currents of the North Atlantic Subtropical Gyre, J Geophys Res Oceans, 128, https://doi.org/10.1029/2022JC019487, 2023.

Peterson, R. G. and Stramma, L.: Upper-level circulation in the South Atlantic Ocean, Prog Oceanogr, 26, 1–73, https://doi.org/10.1016/0079-6611(91)90006-8, 1991.

1120 Petit, T., Mercier, H., and Thierry, V.: New Insight Into the Formation and Evolution of the East Reykjanes Ridge Current and Irminger Current, J Geophys Res Oceans, 124, 9171–9189, https://doi.org/10.1029/2019JC015546, 2019.

Piecuch, C. G.: Likely weakening of the Florida Current during the past century revealed by sea-level observations, Nat Commun, 11, 3973, https://doi.org/10.1038/s41467-020-17761-w, 2020.

Pollard, R. T., Read, J. F., Holliday, N. P., and Leach, H.: Water masses and circulation pathways through the Iceland Basin
1125 during Vivaldi 1996, J Geophys Res, 109, C04004, https://doi.org/10.1029/2003JC002067, 2004.

Polyakov, I. v., Pnyushkov, A. v., Alkire, M. B., Ashik, I. M., Baumann, T. M., Carmack, E. C., Goszczko, I., Guthrie, J., Ivanov, V. v., Kanzow, T., Krishfield, R., Kwok, R., Sundfjord, A., Morison, J., Rember, R., and Yulin, A.: Greater role for Atlantic inflows on sea-ice loss in the Eurasian Basin of the Arctic Ocean, Science (1979), 356, 285–291, https://doi.org/10.1126/science.aai8204, 2017.

1130 Polyakov, I. v., Rippeth, T. P., Fer, I., Alkire, M. B., Baumann, T. M., Carmack, E. C., Ingvaldsen, R., Ivanov, V. v., Janout, M., Lind, S., Padman, L., Pnyushkov, A. v., and Rember, R.: Weakening of Cold Halocline Layer Exposes Sea Ice to Oceanic Heat in the Eastern Arctic Ocean, J Clim, 33, 8107–8123, https://doi.org/10.1175/JCLI-D-19-0976.1, 2020.

Rahmstorf, S.: On the freshwater forcing and transport of the Atlantic thermohaline circulation, Clim Dyn, 12, 799–811, https://doi.org/10.1007/s003820050144, 1996.

1135 Rhein, M., Mertens, C., and Roessler, A.: Observed Transport Decline at 47°N, Western Atlantic, J Geophys Res Oceans, 124, 4875–4890, https://doi.org/10.1029/2019jc014993, 2019.

Rossby, T., Flagg, C. N., Donohue, K., Sanchez-Franks, A., and Lillibridge, J.: On the long-term stability of Gulf Stream transport based on 20 years of direct measurements, Geophys Res Lett, 41, 114–120, https://doi.org/10.1002/2013GL058636, 2014.

1140 Sarafanov, A., Falina, A., Mercier, H., Sokov, A., Lherminier, P., Gourcuff, C., Gladyshev, S., Gaillard, F., and Daniault, N.: Mean full-depth summer circulation and transports at the northern periphery of the Atlantic Ocean in the 2000s, J Geophys Res Oceans, 117, https://doi.org/10.1029/2011JC007572, 2012.

Saunders, P. M. and King, B. A.: Oceanic fluxes on the WOCE A11 section, J Phys Oceanogr, 25, 1942–1958, 1995.

Schmid, C. and Majumder, S.: Transport variability of the Brazil Current from observations and a data assimilation model, 1145 Ocean Science, 14, 417–436, https://doi.org/10.5194/os-14-417-2018, 2018.

Schmitz, W. J. and McCartney, M. S.: On the North Atlantic circulation, Reviews of Geophysics, 31, 29–49, 1993.

Schmitz, W. J., Thompson, J. D., and Luyten, J. R.: The Sverdrup circulation for the Atlantic along 24°N, J Geophys Res, 97, 7251, https://doi.org/10.1029/92JC00417, 1992.

Schott, F. A., Dengler, M., Zantopp, R., Stramma, L., Fischer, J., and Brandt, P.: The Shallow and Deep Western Boundary 1150 Circulation of the South Atlantic at 5°–11°S, J Phys Oceanogr, 35, 2031–2053, https://doi.org/10.1175/jpo2813.1, 2005.

Siedler, G., Müller, T. J., R.Onken, Arhan, M., Mercier, H., King, B. A., and Saunders, P. M.: The Zonal WOCE Sections in the South Atlantic, in: The South Atlantic: present and past circulation, edited by: Wefer, G., Berger, W. H., Siedler, G., and Webb, D. J., Springer-Verlag, Berlin, 83–104, https://doi.org/10.1007/978-3-642-80353-6_5, 1996.

Smythe-Wright, D., Chapman, P., Rae, C. D., Shannon, L. V., and Boswell, S. M.: Characteristics of the South Atlantic 1155 subtropical frontal zone between 15°W and 5°E, Deep Sea Research Part I: Oceanographic Research Papers, 45, 167–192, https://doi.org/10.1016/S0967-0637(97)00068-X, 1998.

Sokolov, S. and Rintoul, S. R.: Circumpolar structure and distribution of the Antarctic Circumpolar Current fronts: 1. Mean circumpolar paths, J Geophys Res, 114, C11018, https://doi.org/10.1029/2008JC005108, 2009.

Spadone, A. and Provost, C.: Variations in the Malvinas Current volume transport since October 1992, J Geophys Res, 114, 1160 C02002, https://doi.org/10.1029/2008JC004882, 2009.

Stendardo, I., Rhein, M., and Steinfeldt, R.: The North Atlantic Current and its Volume and Freshwater Transports in the Subpolar North Atlantic, Time Period 1993–2016, J Geophys Res Oceans, 125, https://doi.org/10.1029/2020JC016065, 2020.

Stramma, L.: The Brazil current transport south of 23°S, Deep Sea Research Part A. Oceanographic Research Papers, 36, 639–646, https://doi.org/10.1016/0198-0149(89)90012-5, 1989.

Stramma, L. and England, M.: On the water masses and mean circulation of the South Atlantic Ocean, J Geophys Res Oceans, 104, 20863–20883, https://doi.org/10.1029/1999JC900139, 1999.

Stramma, L., Ikeda, Y., and Peterson, R. G.: Geostrophic transport in the Brazil current region north of 20°S, Deep Sea Research Part A. Oceanographic Research Papers, 37, 1875–1886, https://doi.org/10.1016/0198-0149(90)90083-8, 1990.

Talley, L. D.: Freshwater transport estimates and the global overturning circulation: Shallow, deep and throughflow components, Prog Oceanogr, 78, 257–303, https://doi.org/10.1016/j.pocean.2008.05.001, 2008.

Talley, L. D., Feely, R. A., Sloyan, B. M., Wanninkhof, R., Baringer, M. O., Bullister, J. L., Carlson, C. A., Doney, S. C., Fine, R. A., Firing, E., Gruber, N., Hansell, D. A., Ishii, M., Johnson, G. C., Katsumata, K., Key, R. M., Kramp, M., Langdon, C., Macdonald, A. M., Mathis, J. T., McDonagh, E. L., Mecking, S., Millero, F. J., Mordy, C. W., Nakano, T., Sabine, C. L., Smethie, W. M., Swift, J. H., Tanhua, T., Thurnherr, A. M., Warner, M. J., and Zhang, J.-Z.: Changes in ocean heat, carbon content, and ventilation: A review of the first decade of GO-SHIP global repeat hydrography, Ann Rev Mar Sci, 8, 185–215, https://doi.org/10.1146/annurev-marine-052915-100829, 2016.

Tuchen, F. P., Brandt, P., Lübbecke, J. F., and Hummels, R.: Transports and Pathways of the Tropical AMOC Return Flow From Argo Data and Shipboard Velocity Measurements, J Geophys Res Oceans, 127, https://doi.org/10.1029/2021JC018115, 2022.

Våge, K., Pickart, R. S., Spall, M. A., Valdimarsson, H., Jónsson, S., Torres, D. J., Østerhus, S., and Eldevik, T.: Significant role of the North Icelandic Jet in the formation of Denmark Strait overflow water, Nat Geosci, 4, 723–727, https://doi.org/10.1038/ngeo1234, 2011a.

Våge, K., Pickart, R. S., Sarafanov, A., Knutsen, Ø., Mercier, H., Lherminier, P., van Aken, H. M., Meincke, J., Quadfasel, D., and Bacon, S.: The Irminger Gyre: Circulation, convection, and interannual variability, Deep Sea Research Part I: Oceanographic Research Papers, 58, 590–614, https://doi.org/10.1016/j.dsr.2011.03.001, 2011b.

Valla, D., Piola, A. R., Meinen, C. S., and Campos, E.: Strong Mixing and Recirculation in the Northwestern Argentine Basin, J Geophys Res Oceans, 123, 4624–4648, https://doi.org/10.1029/2018JC013907, 2018.

Vélez-Belchí, P., Pérez-Hernández, M. D., Casanova-Masjoan, M., Cana, L., and Hernández-Guerra, A.: On the seasonal variability of the Canary Current and the Atlantic Meridional Overturning Circulation, J Geophys Res Oceans, 122, 4518–4538, https://doi.org/10.1002/2017JC012774, 2017.

Vivier, F. and Provost, C.: Direct velocity measurements in the Malvinas Current, J Geophys Res Oceans, 104, 21083–21103, https://doi.org/10.1029/1999JC900163, 1999a.

Vivier, F. and Provost, C.: Volume transport of the Malvinas Current: Can the flow be monitored by TOPEX/POSEIDON?, J Geophys Res Oceans, 104, 21105–21122, https://doi.org/10.1029/1999JC900056, 1999b.

Wedepohl, P. M., Lutjeharms, J. R. E., and Meeuwis, M.: Surface drift in the South-East Atlantic Ocean, South African Journal of Marine Science, 22, 71–79, https://doi.org/10.2989/025776100784125672, 2000.

Weijer, W., Cheng, W., Drijfhout, S. S., Fedorov, A. V., Hu, A., Jackson, L. C., Liu, W., McDonagh, E. L., Mecking, J. V., and Zhang, J.: Stability of the Atlantic Meridional Overturning Circulation: A Review and Synthesis, J Geophys Res Oceans, 124, 5336–5375, https://doi.org/10.1029/2019JC015083, 2019.

Wunsch, C.: The North Atlantic General Circulation West of 50ºW Determined by Inverse Methods, Reviews of Geophysics and Space Physics, 16, 583–620, 1978.

Wunsch, C.: The Ocean Circulation Inverse Problem, Cambridge University Press, Cambridge, USA, 464 pp., 1996.

Wunsch, C. and Heimbach, P.: Estimated Decadal Changes in the North Atlantic Meridional Overturning Circulation and Heat Flux 1993–2004, J Phys Oceanogr, 36, 2012–2024, https://doi.org/10.1175/JPO2957.1, 2006.

Yashayaev, I. and Loder, J. W.: Recurrent replenishment of Labrador Sea Water and associated decadal-scale variability, J Geophys Res Oceans, 121, 8095–8114, https://doi.org/10.1002/2016JC012046, 2016.

Yashayaev, I. and Loder, J. W.: Further intensification of deep convection in the Labrador Sea in 2016, Geophys Res Lett, 44, 1429–1438, https://doi.org/10.1002/2016GL071668, 2017.

Zantopp, R., Fischer, J., Visbeck, M., and Karstensen, J.: From interannual to decadal: 17 years of boundary current transports at the exit of the Labrador Sea, J Geophys Res Oceans, 122, 1724–1748, https://doi.org/10.1002/2016JC012271, 2017.

Zenk, W. and Morozov, E.: Decadal warming of the coldest Antarctic Bottom Water flow through the Vema Channel, Geophys Res Lett, 34, L14607, https://doi.org/10.1029/2007GL030340, 2007.
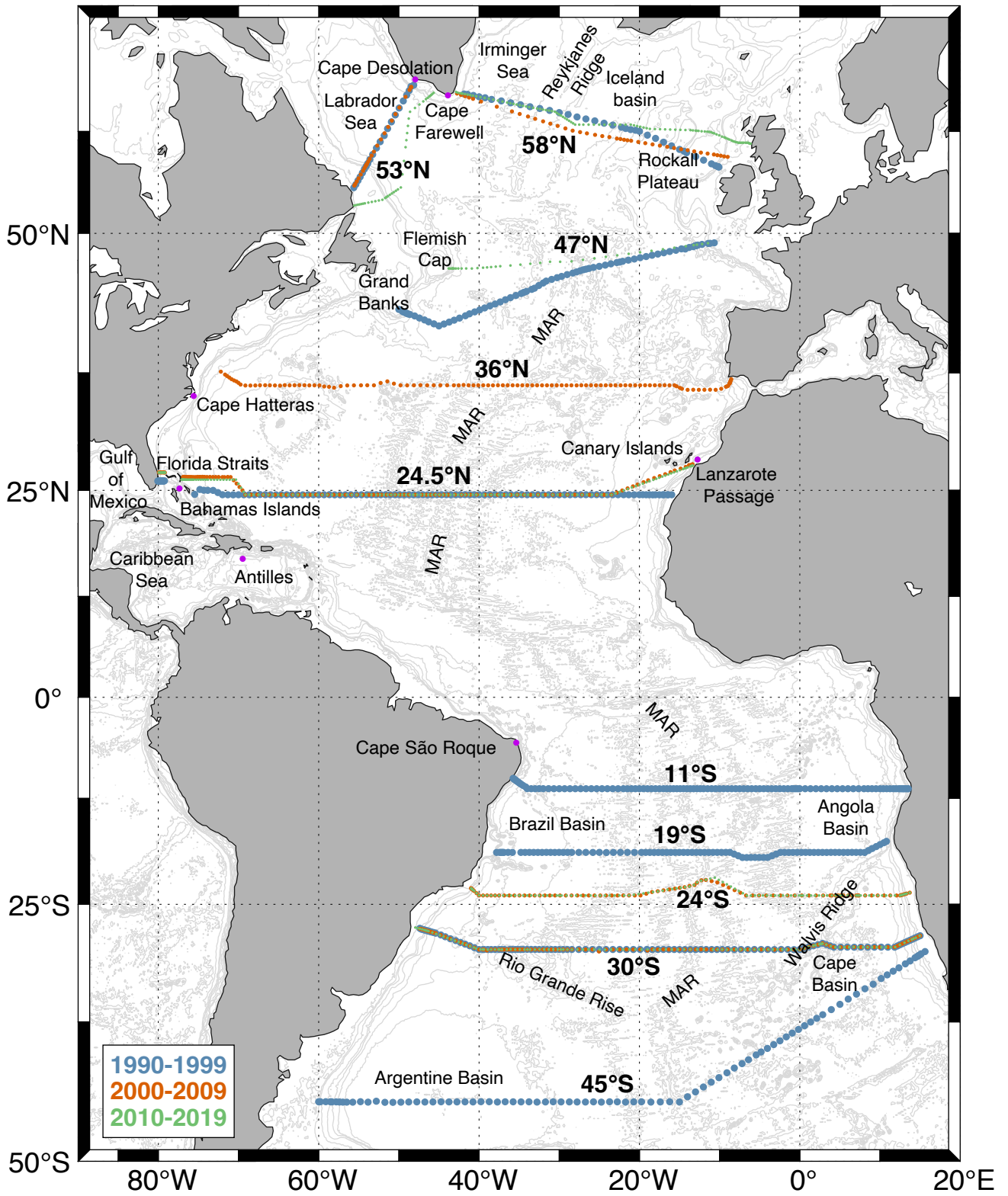
Figure 1: Map of the zonal sections in each decade for the inverse model. Each section is accompanied by its nominal latitude, with colours representing the combination of cruises used for each decade, blue for 1990-1999, orange for 2000-2009, and green for 2010-2019. The main geographical features are included in the figure.

1225

MASS TRANSPORT (Sv)

EGC
-0.4 ± 0.6
-1.6 ± 1.8
-3.3 ± 1.0

uWGC
1.3 ± 0.4
1.6 ± 1.0
3.4 ± 1.0

IC
5.0 ± 2.7
4.7 ± 1.9
6.1 ± 1.2

ERRC
-3.2 ± 2.2
-1.8 ± 1.4
-2.0 ± 0.8

NAC
5.2 ± 3.7
5.4 ± 2.7
6.7 ± 1.6

LC
-5.2 ± 0.9
-8.4 ± 3.9
-11.4 ± 6.8

dWGC
5.4 ± 1.0
5.8 ± 1.1
8.8 ± 1.5

DSOW
-4.9 ± 7.8
-5.5 ± 6.8
-6.2 ± 4.9

DSOW
-3.7 ± 8.2
-2.4 ± 8.0
-0.9 ± 4.6

ISOW
-10.8 ± 6.5
-9.6 ± 5.3
-10.0 ± 3.0

LC
-2.1 ± 0.5
-1.2 ± 0.4
-1.6 ± 0.4

DWBC
-30.1 ± 10.4
-37.5 ± 5.7

NAC
33.4 ± 2.9
28.2 ± 1.5

GS
74.9 ± 1.7

DWBC
-34.5 ± 8.7

FC
34.5 ± 0.3
32.1 ± 0.3
31.3 ± 0.3

AC
12.8 ± 1.0
13.2 ± 0.4
7.5 ± 0.3

CC
-5.1 ± 0.9
-6.1 ± 1.4
-4.8 ± 0.7

AABW
0.1 ± 0.9
0.7 ± 0.9
0.3 ± 1.3

DWBC
-23.8 ± 10.8
-18.3 ± 9.8
-30.4 ± 7.3

NBrC
17.0 ± 1.2

DWBC
-17.3 ± 2.2

AABW
1.2 ± 1.2

BrC
-19.7 ± 1.3

DWBC
-20.8 ± 7.2

AABW
1.9 ± 1.4

SEC
9.0 ± 1.9

BeC
2.3 ± 1.2

BrC
-4.7 ± 0.4
-12.0 ± 0.7

DWBC
-29.0 ± 9.0
-27.5 ± 7.1

AABW
0.5 ± 2.3
1.9 ± 2.0

DEBC
-13.7 ± 5.5
-9.7 ± 6.1

SEC
16.5 ± 1.7
16.5 ± 1.6

BeC
8.7 ± 1.3
4.6 ± 0.8

BrC
-26.7 ± 1.6
-22.2 ± 1.5
-9.5 ± 0.7

DWBC
-26.6 ± 5.1
-25.9 ± 5.0
-27.9 ± 1.9

AABW
3.9 ± 1.3
3.3 ± 1.3
3.5 ± 1.5

DEBC
-8.3 ± 5.7
-9.7 ± 3.5
-8.6 ± 3.4

SEC
16.9 ± 1.9
14.6 ± 2.1
15.9 ± 1.9

BeC
12.1 ± 1.2
12.1 ± 1.2
13.5 ± 1.0

BeC
24.0 ± 2.3

DEBC
-6.4 ± 6.3

MC
37.2 ± 2.0

AABW
4.7 ± 1.5

DWBC
-49.1 ± 7.0

ACC
-55.5 ± 5.6

Upper
Deep
Bottom

1990-1999
2000-2009
2010-2019

Figure 2: Circulation in the upper, deep and abyssal layers in the Atlantic Ocean for mass transport (Sv). The background arrows represent the circulation of the main currents in the text, in red for surface layers, purple for deep and blue for abyssal. At each section, the mass transports (in Sv) for each current appear in a box, with values in blue for the solutions for the 1990-1999 model, orange for 2000-2009 model solutions, and green for 2010-2019 model solutions. Surface currents include Antilles Current (AC), Benguela Current (BeC), Antarctic Circumpolar Current (ACC), Brazil Current (BrC), Canary Current (CC), East Greenland Current (EGC), East Reykjanes Ridge Current (ERRC), Florida Current (FC), Gulf Stream (GS), Irminger Current (IC), Labrador Current (LC), Malvinas Current (MC), North Atlantic Current (NAC), North Brazil Current (NBrC), South Equatorial Current (SEC) and Upper West Greenland Current (uWGC). Deep currents are comprised of Deep Eastern Boundary Current (DEBC), Deep West Greenland Current (dWGC), Deep, Western Boundary Current (DWBC), Denmark Strait Overflow Water (DSOW), Iceland-Scotland Overflow Water (ISOW) and Labrador Current (LC). Abyssal layers are configured by the distribution of Antarctic Bottom Water (AABW).
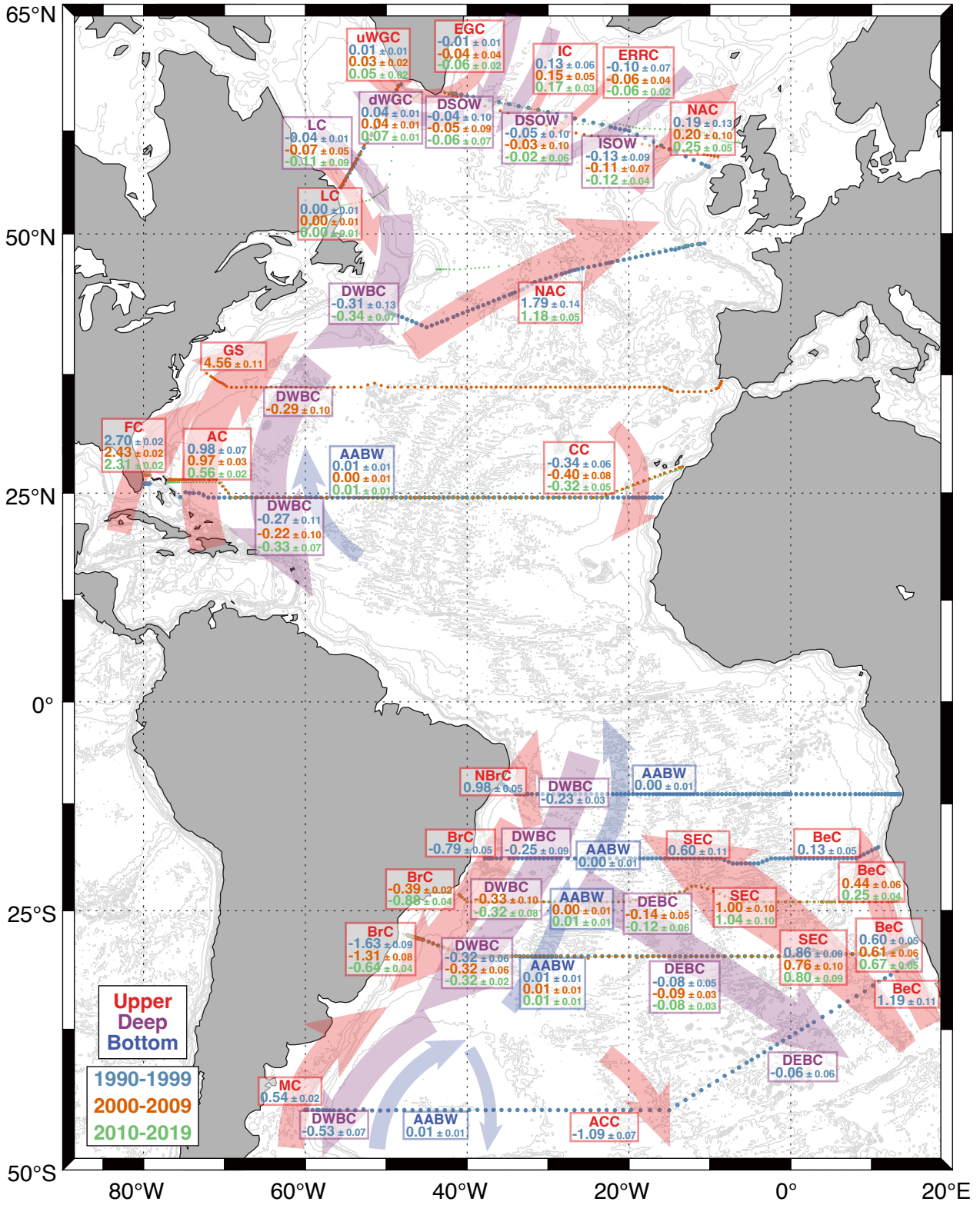
HEAT TRANSPORT (PW)

Figure 3: Same as Figure 2 but for heat transport (PW).

FRESHWATER FLUX (Sv)
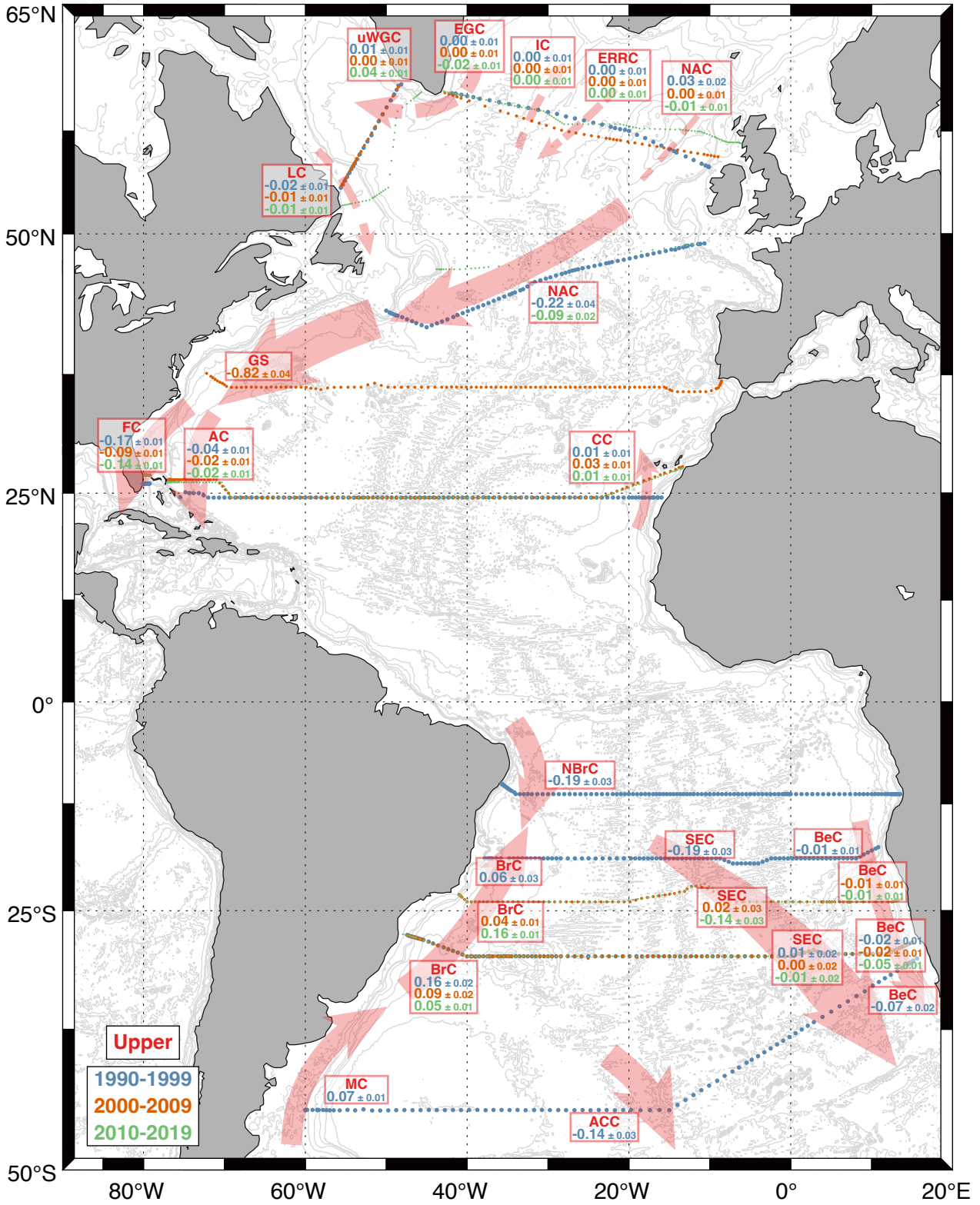
Figure 4: Same as Figure 2 but for freshwater transport (Sv) in upper layers

SOUTH ATLANTIC
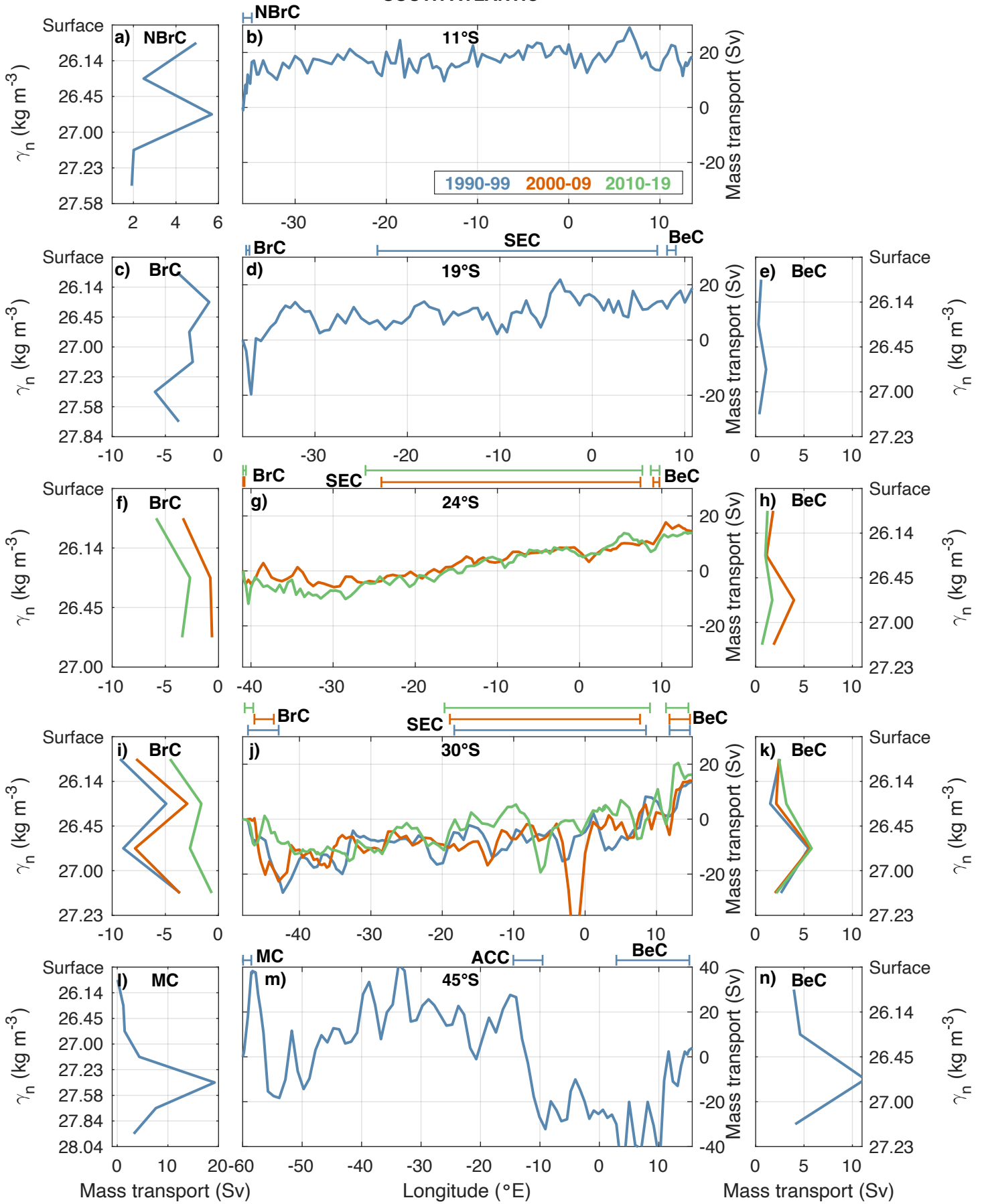
Figure 5: South Atlantic currents at different latitudes and decades. Net mass transport (Sv) per layer defined between neutral density interfaces for North Brazil Current (NBrC) at 11°S (a), Brazil Current (BrC) at 19°S (c), 24°S (f) and 30°S (i), for the Benguela Current System (BeC) at 19°S (e), 24°S (h), 30°S (k) and 45°S (n) and for Malvinas Current (MC) at 45°S (l). The transport per layer is computed using the stations and layers specified in Table 2. The longitudinal ranges of the currents at each latitude appear on the top of the middle panel. Different colours denote the use of the model solutions in blue for 1990-1999, orange for 2000-2009, and green for 2010-2019. The middle panels show the eastward accumulated horizontal mass transport (Sv) for upper layers for the 11°S (b), 19°S (d), 24°S (g), 30°S (j) and 45°S (m) sections.
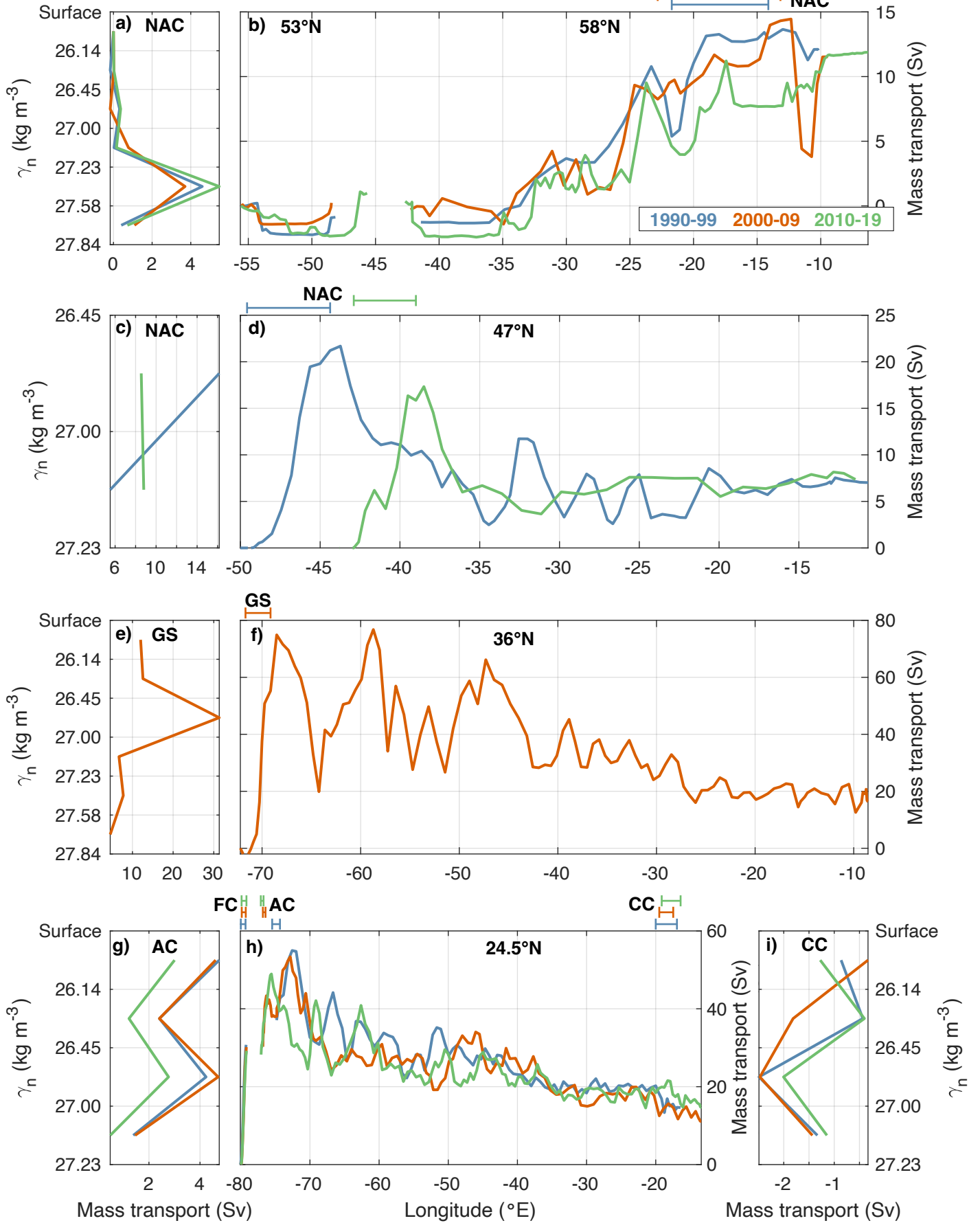
1255

Figure 6: Surface currents in the north Atlantic at different latitudes and decades. Net mass transport (Sv) per layer defined between neutral density interfaces for the northward North Atlantic Current (NAC) at 47°N (a) and 53°N+58°N (c), Gulf Stream (GS) at 36°N (e), Antilles Current (AC) at 24.5°N (g) and for the southward Canary Current (CC) at 24.5°N (i). The transport per layer is computed using the stations and layers specified in Table 2. The longitudinal ranges of the currents at each latitude appear on the top of the middle panel. Different colours denote the use of the model solutions in blue for 1990-1999, orange for 2000-2009, and green for 2010-2019. The right panels show the eastward accumulated horizontal mass transport (Sv) for upper layers for the 58°N (b), 47°N (d), 36°N (f) and 24.5°N (h) sections.

SUBPOLAR NORTH ATLANTIC
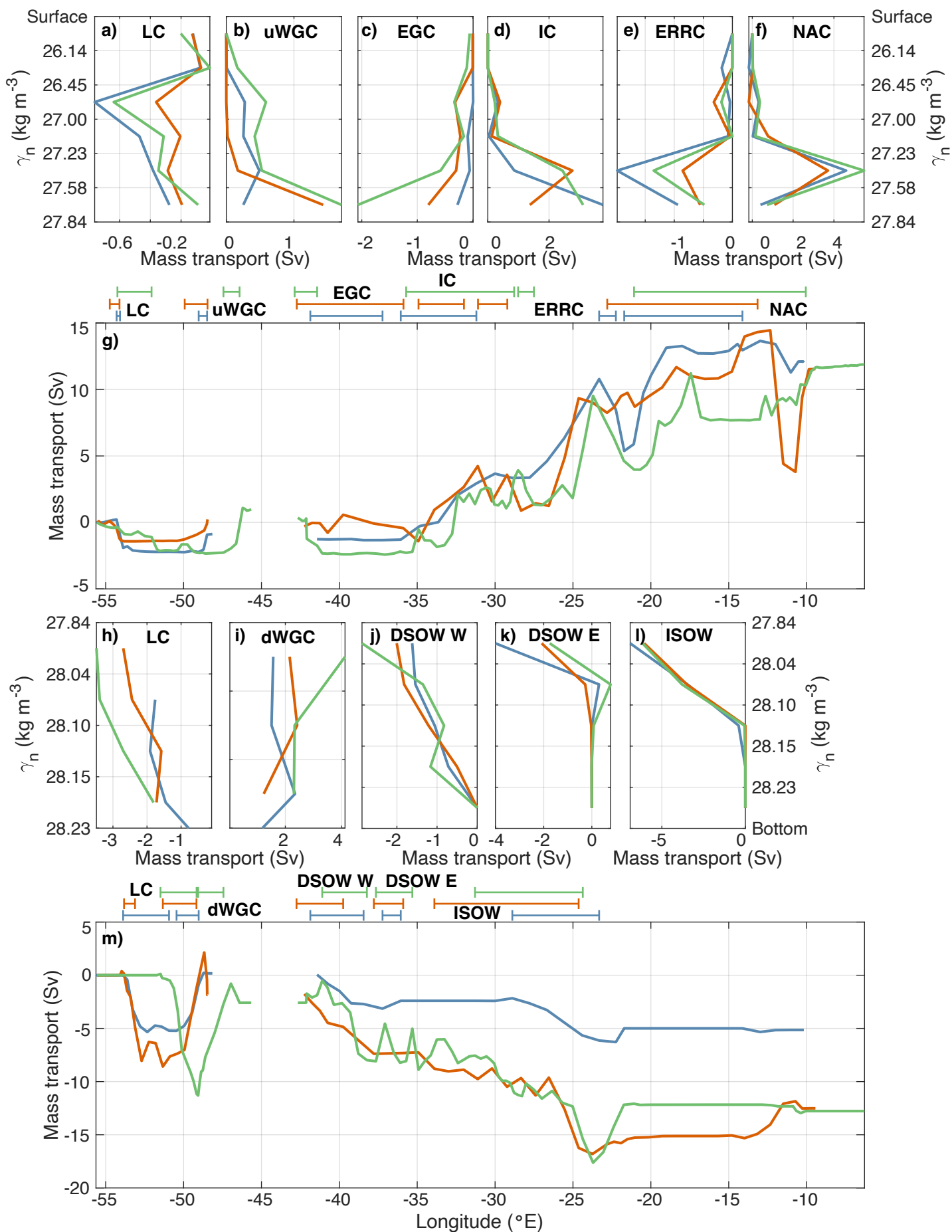
Figure 7: Upper and deep currents in the subpolar North Atlantic at 53°N+58°N for the three decades. Net mass transport (Sv) per layer defined between neutral density interfaces at 53°N+58°N for upper layers: upper Labrador Current (LC; a), upper West Greenland Current (uWGC; b), East Greenland Current (EGC; c) Irminger Current (IC; d), East Reykjanes Ridge Current (ERRC; e) and North Atlantic Current (NAC; f), as well as for deep layers: deep Labrador Current (LC; h), deep West Greenland Current (dWGC; i), west and east Denmark Strait Overflow Waters (DSOW; j and k) and Iceland-Scotland Overflow Waters (ISOW; l). The transport per layer is computed using the stations and layers specified in Tables 2 and 3. The longitudinal ranges of the currents at each latitude appear on the top of the middle panel. Different colours denote the use of the model solutions in blue for 1990-1999, orange for 2000-2009, and green for 2010-2019. The panels below the vertical net transport show the eastward accumulated horizontal mass transport (Sv) at 53°N+58°N for upper (g) and deep (m) layers.
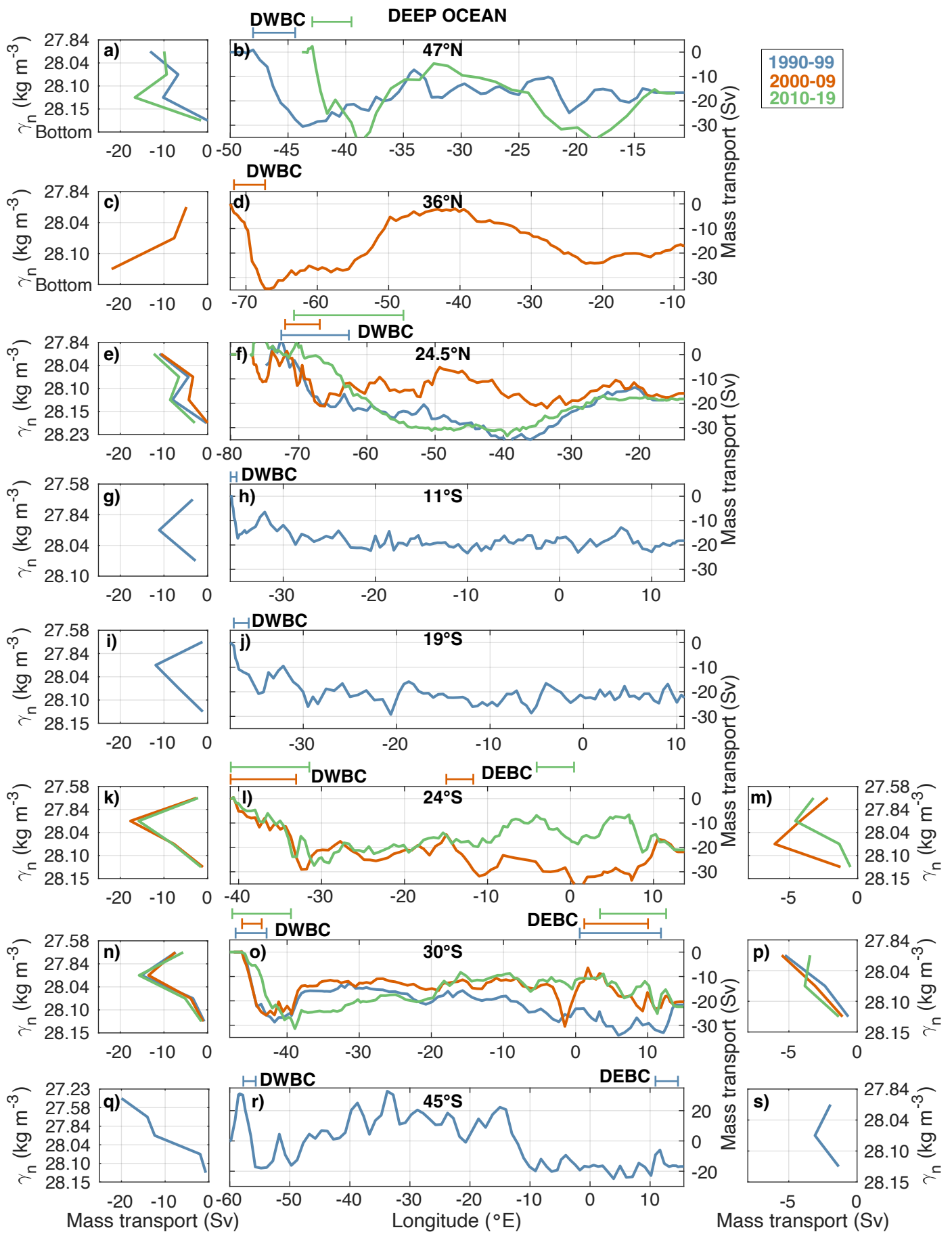
Figure 8: Deep boundary currents of the Atlantic at different latitudes and decades. Net mass transport (Sv) per layer defined between neutral density interfaces for Deep Western Boundary Current (DWBC) at 47°N (a), 36°N (c), 24.5°N (e), 11°S (g), 19°S (i), 24°S (k), 30°S (n) and 45°S (q) and for Deep Eastern Boundary Current (DEBC) at 24°S (m), 30°S (p) and 45°S (s). The transport per layer is computed using the stations and layers specified in Table 3. The longitudinal ranges of the currents at each latitude appear on the top of the middle panel. Different colours denote the use of the model solutions in blue for 1990-1999, orange for 2000-2009, and green for 2010-2019. he middle panels show the eastward accumulated horizontal mass transport (Sv) for deep layers for the 47°N (b), 36°N (d), 24.5°N (f), 11°S (h), 19°S (j), 24°S (l), 30°S (o) and 45°S (r) sections.
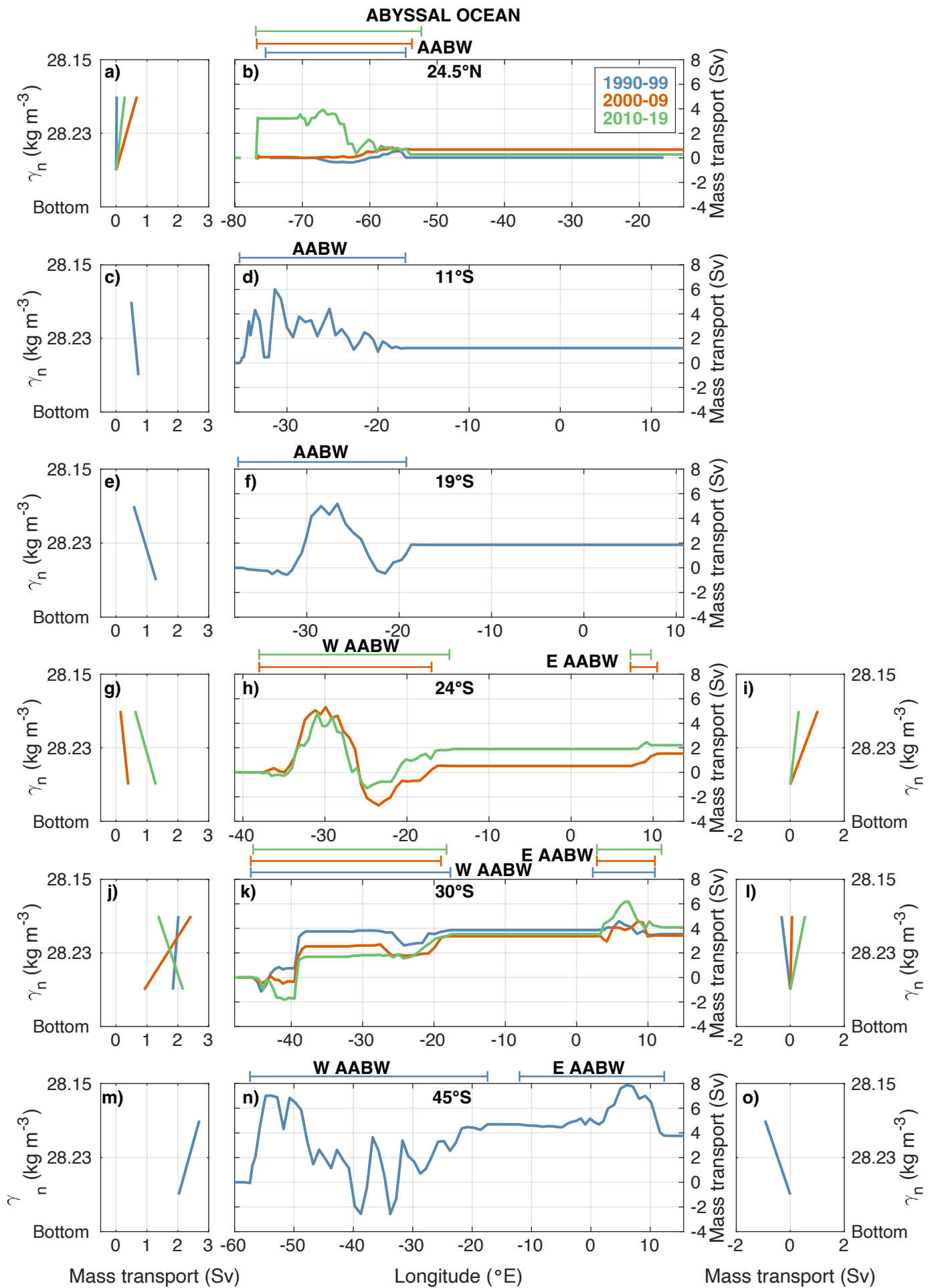
Figure 9: Abyssal currents in the Atlantic at different latitudes and decades. Net mass transport (Sv) per layer defined between neutral density interfaces for the Antarctic Bottom Water (AABW) West of the MAR at 24.5°N (a), 11°S (c), 19°S (e), 24°S (g), 30°s (j), and 45°S (m), and East of the MAR at 24°S (i), 30°s (l), and 45°S (o). The transport per layer is computed using the stations and layers specified in Table 4. The longitudinal ranges of the currents at each latitude appear on the top of the middle panel. Different colours denote the use of the model solutions in blue for 1990-1999, orange for 2000-2009, and green for 2010-2019. The middle panels show the eastward accumulated horizontal mass transport (Sv) for upper layers for the 24.5°N (b), 11°S (d), 19°S (f), 24°S (h), 30°s (k), and 45°S (n) sections.

Table 1: Zonal sections used for each decade, including the reference layer where no-motion is assumed. The Ekman transport is computed for the time of the cruise using the corresponding wind stress NCEP-NCAR product.

Section	Year	Cruise ID	Dates	Latitude	Country	Reference	No stns	Ref. layer	T_{Ek} (Sv)
A11	1992-93	74DI19921222	27 Dec – 30 Jan	30-45°S	UK	Saunders and King (1995)	91	28.15	1.5 ± 0.2
A10	1992-93	06MT19921227	30 Dec – 28 Jan	30°S	DE	Siedler et al. (1996)	110	28.15	-0.17 ± 0.09
A09	1991	06MT19910210	12 Feb – 18 Mar	19°S	DE	Siedler et al. (1996)	89	28.15	-2.5 ± 0.1
A08	1994	06MT19940329	01 Apr – 07 May	11°S	DE	Siedler et al. (1996)	110	27.58-28.10	-4.6 ± 0.2
A05	1992	29HE19920714	20 Jul – 14 Aug	24.5°N	SP	Parrilla et al. (1994)	11+99	28.15	3.1 ± 0.1
A02	1993	06GA19930612	08 Jul – 25 Jul	40-50°N	DE	Koltermann et al. (1999)	74	28.15	-0.30 ± 0.08
AR07W	1990	18DA90012	06 Jul – 09 Jul	55-60°N	CA	Lazier et al. (2002)	22	27.84	-0.01 ± 0.02
AR07E	1991	74AB62	08 Aug – 03 Sep	55-60°N	UK	Våge et al. (2011)	38	27.84	-0.40 ± 0.06
A10	2003	49NZ20031106	07 Nov – 02 Dec	30°S	JA	Katsumata and Fukasawa (2011)	111	28.15	-0.2 ± 0.1
A095	2009	740H20090307	16 Mar – 19 Apr	24°S	UK	Johns et al. (2011)	94	28.15	-1.5 ± 0.1
A05	2004	74DI20040404	07 Apr – 09 May	24.5°N	UK	Bryden et al. (2005)	9+115	28.04	2.1 ± 0.2
A03	2005	74AB20050501	03 May – 12 Jun	36°N	UK	McDonagh et al. (2010)	112	28.04	-0.00 ± 0.02
AR07W	2005	18HU20050526	29 May – 03 Jun	55-60°N	CA	Bersch et al. (2007); Våge et al. (2011)	24	27.84	-0.007 ± 0.008
AR07E	2007	64PE20070830	12 Sep – 22 Sep	55-60°N	NE	Yashayaev and Loder (2017, 2016)	42	27.84	-0.80 ± 0.08
A10	2011	33RO20110926	28 Sep – 29 Oct	30°S	US	Hernández-Guerra et al. (2019)	120	28.15	-0.3 ± 0.1
A095	2018	740H20180228	02 Mar – 05 Apr	19°S	UK	King et al. (2019)	117	28.15	-0.9 ± 0.1
A05	2011	29AH20110128	28 Jan – 11 Mar	24.5°N	SP	Hernández-Guerra et al. (2014)	14+152	28.04	2.1 ± 0.2
A02	2013	06M220130509	29 May – 14 Jun	40-50°N	DE	Rhein et al. (2019)	39	27.84	-0.26 ± 0.07
AR07W	2014	74JC20140606	09 Jun – 18 Jun	55-60°N	UK	Lozier et al. (2019)	40	27.84	-0.16 ± 0.04
AR07E	2014	74JC20140606	24 Jun – 17 Jul	55-60°N	UK	Lozier et al. (2019)	103	27.84	0.02 ± 0.03

305

Table 2: Characteristics of each upper-layer current found at every section.

Decade	Stations	Long (°E)	Dist (km)	Layers	Depth (m)	Mass Trans (Sv)	Heat Trans (PW)	Fw Total (Sv)	TWT (°C)	TWS
Malvinas Current 45°S										
1990-99	1:5	-59.9:-58.6	109	1:7	0 to 1206	37.2 ± 2.0	0.54 ± 0.02	0.07 ± 0.01	3.66	34.265
Brazil Current 30°S										
1990-99	1:15	-47.2:-42.9	443	1:4	0 to 678	-26.7 ± 1.6	-1.63 ± 0.09	0.16 ± 0.02	15.47	35.611
2000-09	6:14	-46.3:-43.6	282	1:4	0 to 735	-22.2 ± 1.5	-1.31 ± 0.08	0.09 ± 0.02	14.96	35.558
2010-19	1:7	-47.7:-46.5	122	1:4	0 to 505	-9.5 ± 0.7	-0.64 ± 0.04	0.05 ± 0.01	16.99	35.900
Brazil Current Recirculation 30°S										
1990-99	16:20	-41.7:-40.0	180	1:4	0 to 1207	16.4 ± 1.9	0.85 ± 0.07	-0.16 ± 0.03	13.09	35.300
2000-09	15:17	-42.3:-41.7	60	1:4	0 to 1187	15.9 ± 2.0	0.80 ± 0.08	-0.14 ± 0.03	12.75	35.248
2010-19	8:10	-45.8:-45.4	49	1:4	0 to 764	13.2 ± 1.4	0.76 ± 0.07	-0.06 ± 0.02	14.54	35.271
Brazil Current 24°S										
2000-09	1:5	-41.0:-40.8	25	1:3	0 to 476	-4.7 ± 0.4	-0.39 ± 0.02	0.04 ± 0.01	21.03	36.340
2010-19	1:6	-41.0:-40.6	47	1:3	0 to 515	-12.0 ± 0.7	-0.88 ± 0.04	0.16 ± 0.01	18.64	36.066
Brazil Current Recirculation 24°S										
2000-09	6:10	-40.3:-39.0	136	1:4	0 to 719	8.9 ± 1.4	0.57 ± 0.09	-0.03 ± 0.03	16.17	35.617
2010-19	7:8	-40.3:-40.0	43	1:4	0 to 738	10.5 ± 0.9	0.70 ± 0.05	-0.07 ± 0.02	16.69	35.785
Brazil Current 19°S										
1990-99	1:4	-37.4:-37.1	37	1:6	0 to 1514	-19.7 ± 1.3	-0.79 ± 0.05	0.06 ± 0.03	10.21	35.113
Brazil Current Recirculation 19°S										
1990-99	5:6	-36.7:-36.4	25	1:6	0 to 1490	19.3 ± 2.1	0.67 ± 0.08	0.06 ± 0.04	8.79	34.863
Antarctic Circumpolar Current Front 45°S										
1990-99	51:57	-15.0:-10.1	463	1:8	0 to 3035	-55.5 ± 5.6	-1.09 ± 0.07	-0.14 ± 0.03	4.96	34.471
Benguela Current 45°S										
1990-99	72:90	2.9:15.1	1335	1:4	0 to 650	24.0 ± 2.3	1.19 ± 0.11	-0.07 ± 0.02	12.53	35.057
Benguela Current 30°S										
1990-99	99:109	11.8:14.7	304	1:4	0 to 496	12.1 ± 1.2	0.60 ± 0.05	-0.02 ± 0.01	12.66	34.998
2000-09	100:110	11.8:14.7	306	1:4	0 to 523	12.1 ± 1.2	0.61 ± 0.06	-0.02 ± 0.01	12.75	35.071
2010-19	111:119	11.3:14.5	326	1:4	0 to 528	13.5 ± 1.0	0.67 ± 0.05	-0.05 ± 0.01	12.66	35.102

.310

Benguela Current 24°S								
2000-09	82:84	9.0:9.7	76	1:4	0 to 540	8.7 ± 1.3	0.44 ± 0.06	12.69	35.019
2010-19	103:106	8.7:9.7	108	1:4	0 to 552	4.6 ± 0.8	0.25 ± 0.04	13.94	35.096
Benguela Current 19°S								
1990-99	82:85	8.1:9.0	113	1:4	0 to 500	2.3 ± 1.2	0.13 ± 0.05	14.06	35.262
South Equatorial Current 30°S								
1990-99	57:96	-18.4:8.5	2587	1:4	0 to 696	16.9 ± 1.9	0.86 ± 0.09	12.85	35.060
2000-09	57:96	-19.0:7.6	2565	1:4	0 to 736	14.6 ± 2.1	0.76 ± 0.10	13.22	35.142
2010-19	58:108	-19.8:9.0	2773	1:4	0 to 727	15.9 ± 1.9	0.80 ± 0.09	12.70	35.179
South Equatorial Current 24°S								
2000-09	32:81	-24.2:7.4	3201	1:4	0 to 620	16.5 ± 1.7	1.00 ± 0.10	15.35	35.451
2010-19	34:102	-26.1:7.6	3421	1:4	0 to 634	16.5 ± 1.6	-0.14 ± 0.03	15.94	35.537
South Equatorial Current 19°S								
1990-99	25:81	-23.2:7.0	3181	1:4	0 to 515	9.0 ± 1.9	0.60 ± 0.11	16.90	35.644
North Brazil Current 11°S								
1990-99	1:10	-35.7:-34.7	130	1:5	0 to 937	17.0 ± 1.2	0.98 ± 0.05	14.59	35.509
Florida Current 24.5°N								
1990-99	1:10	-80.0:-79.3	68	1:6	0 to 511	34.5 ± 0.3	2.70 ± 0.02	19.84	36.120
2000-09	1:8	-79.9:-79.3	58	1:6	0 to 566	32.1 ± 0.3	2.43 ± 0.02	19.16	36.201
2010-19	1:13	-79.9:-79.2	70	1:6	0 to 592	31.3 ± 0.3	2.31 ± 0.02	18.65	36.098
Antilles Current 24.5°N								
1990-99	11:14	-75.5:-74.3	125	1:4	0 to 736	12.8 ± 1.0	0.98 ± 0.07	19.45	36.394
2000-09	10:17	-76.8:-76.4	38	1:4	0 to 758	13.2 ± 0.4	0.97 ± 0.03	18.67	36.431
2010-19	14:24	-77.1:-76.7	39	1:4	0 to 704	7.5 ± 0.3	0.56 ± 0.02	19.05	36.484
Canary Current 24.5°N								
1990-99	98:107	-20.0:-16.9	310	1:4	0 to 509	-5.1 ± 0.9	-0.34 ± 0.06	16.57	36.283
2000-09	110:114	-19.5:-17.5	215	1:4	0 to 532	-6.1 ± 1.4	-0.40 ± 0.08	16.59	36.313
2010-19	145:153	-19.1:-16.4	289	1:4	0 to 578	-4.8 ± 0.7	-0.32 ± 0.05	16.86	36.372
Gulf Stream 36°N								
2000-09	1:10	-71.7:-69.1	256	1:6	0 to 891	74.9 ± 1.7	4.56 ± 0.11	15.42	36.014

Note: the second trend column values read: -0.01 ± 0.01; -0.01 ± 0.01; -0.01 ± 0.01; 0.01 ± 0.02; 0.00 ± 0.02; -0.01 ± 0.02; 0.02 ± 0.03; -0.14 ± 0.03; -0.07 ± 0.04; -0.19 ± 0.03; -0.17 ± 0.01; -0.09 ± 0.01; -0.14 ± 0.01; -0.04 ± 0.01; -0.02 ± 0.01; -0.02 ± 0.01; 0.01 ± 0.01; 0.03 ± 0.01; 0.01 ± 0.01; -0.82 ± 0.04.

Gulf Stream Recirculation 36°N									
2000-09	10:17	-68.5:-64.8	331	1:6	0 to 1281	-35.4 ± 3.0	-2.29 ± 0.18	0.19 ± 0.05	16.36	36.138
North Atlantic Current 47°N									
1990-99	1:14	-49.6:-44.4	444	1:6	0 to 838	33.4 ± 2.9	1.79 ± 0.14	-0.22 ± 0.04	13.53	35.722
2010-19	7:15	-42.9:-39.0	294	1:6	0 to 982	28.2 ± 1.5	1.18 ± 0.05	-0.09 ± 0.02	10.59	35.368
North Atlantic Current 58°N									
1990-99	42:53	-21.7:-14.1	496	1:6	0 to 1034	5.2 ± 3.7	0.19 ± 0.13	0.03 ± 0.02	9.12	35.290
2000-09	47:61	-22.8:-13.2	599	1:6	0 to 1010	5.4 ± 2.7	0.20 ± 0.10	0.00 ± 0.01	9.27	35.347
2010-19	93:121	-21.1:-10.1	662	1:6	0 to 947	6.7 ± 1.6	0.25 ± 0.05	-0.01 ± 0.01	9.29	35.292
East Reykjanes Ridge Current 58°N									
1990-99	40:42	-23.3:-22.2	66	1:6	0 to 1183	-3.2 ± 2.2	-0.10 ± 0.07	0.00 ± 0.01	8.14	35.131
2000-09	38:41	-31.1:-29.2	117	1:6	0 to 911	-1.8 ± 1.4	-0.06 ± 0.04	0.00 ± 0.01	8.45	35.070
2010-19	80:84	-28.5:-27.5	63	1:6	0 to 929	-2.0 ± 0.8	-0.06 ± 0.02	0.00 ± 0.01	7.79	35.082
Irminger Current 58°N									
1990-99	29:34	-36.1:-31.2	282	1:6	0 to 615	5.0 ± 2.7	0.13 ± 0.06	0.00 ± 0.01	6.37	34.991
2000-09	34:38	-34.9:-32.0	178	1:6	0 to 798	4.7 ± 1.9	0.15 ± 0.05	0.00 ± 0.01	8.12	35.105
2010-19	59:80	-35.7:-28.8	418	1:6	0 to 783	6.1 ± 1.2	0.17 ± 0.03	0.00 ± 0.01	6.91	35.019
East Greenland Current 58°N									
1990-99	22:29	-41.9:-37.2	264	1:6	0 to 194	-0.4 ± 0.6	-0.01 ± 0.01	0.00 ± 0.01	5.94	34.938
2000-09	26:34	-42.8:-35.9	408	1:6	0 to 621	-1.6 ± 1.8	-0.04 ± 0.04	0.00 ± 0.01	6.60	34.826
2010-19	40:48	-42.9:-41.4	82	1:6	0 to 579	-3.3 ± 1.0	-0.06 ± 0.02	-0.02 ± 0.01	4.42	34.560
Upper West Greenland Current 53°N									
1990-99	18:21	-49.0:-48.5	67	1:6	0 to 262	1.3 ± 0.4	0.01 + 0.01	0.01 ± 0.01	2.74	34.126
2000-09	20:25	-49.9:-48.5	164	1:6	0 to 1232	1.6 ± 1.0	0.03 ± 0.02	0.00 ± 0.01	4.62	34.857
2010-19	31:35	-47.4:-46.4	75	1:6	0 to 788	3.4 ± 1.0	0.05 ± 0.02	0.04 ± 0.01	3.57	34.332
Upper Labrador Current 53°N									
1990-99	5:7	-54.3:-54.1	26	1:6	0 to 413	-2.1 ± 0.5	0.00 ± 0.01	-0.02 ± 0.01	0.45	33.569
2000-09	4:8	-54.8:-54.1	80	1:6	0 to 418	-1.2 ± 0.4	0.00 ± 0.01	-0.01 ± 0.01	0.98	33.630
2010-19	6:12	-54.2:-52.1	151	1:6	0 to 400	-1.6 ± 0.4	0.00 ± 0.01	-0.01 ± 0.01	0.22	33.455

Table 3: Characteristics of each deep-layer current found at every section.

Decade	Stations	Long (°E)	Dist (km)	Layers	Depth (m)	Mass Trans (Sv)	Heat Trans (PW)	Fw Total (Sv)	TWT (°C)	TWS
Iceland-Scotland Overflow Waters 58°N										
1990-99	35:41	-28.9:-23.3	335	7:11	2353 to bottom	-10.8 ± 6.5	-0.13 ± 0.09	0.00 ± 0.01	3.07	34.943
2000-09	35:46	-33.9:-24.6	567	7:11	2157 to bottom	-9.6 ± 5.3	-0.11 ± 0.07	0.00 ± 0.01	3.04	34.944
2010-19	70:89	-31.3:-24.4	416	7:11	2037 to bottom	-10.0 ± 3.0	-0.12 ± 0.04	0.01 ± 0.01	3.08	34.958
Denmark Strait Overflow Waters East 58°N										
1990-99	28:30	-37.2:-36.1	68	7:11	2413 to bottom	-3.7 ± 8.2	-0.05 ± 0.10	0.00 ± 0.01	3.28	34.886
2000-09	32:34	-37.8:-35.9	113	7:11	2521 to bottom	-2.4 ± 8.0	-0.03 ± 0.10	0.00 ± 0.01	3.50	34.908
2010-19	55:61	-37.7:-35.3	135	7:11	2511 to bottom	-0.9 ± 4.6	-0.02 ± 0.06	0.00 ± 0.01	4.27	34.955
Denmark Strait Overflow Waters West 58°N										
1990-99	22:28	-41.9:-38.4	195	7:11	2257 to bottom	-4.9 ± 7.8	-0.04 ± 0.10	-0.01 ± 0.01	2.29	34.904
2000-09	26:32	-42.8:-39.8	177	7:11	1760 to bottom	-5.5 ± 6.8	-0.05 ± 0.09	0.00 ± 0.01	2.45	34.911
2010-19	48:55	-41.1:-38.2	164	7:11	2292 to bottom	-6.2 ± 4.9	-0.06 ± 0.07	0.01 ± 0.01	2.54	34.915
Deep West Greenland Current 53°N										
1990-99	15:19	-50.5:-49.0	162	8:11	3302 to bottom	5.4 ± 1.0	0.04 ± 0.01	0.00 ± 0.01	1.84	34.900
2000-09	17:22	-51.3:-49.2	249	8:10	3981 to bottom	5.8 ± 1.1	0.04 ± 0.01	0.00 ± 0.01	1.93	34.888
2010-19	25:32	-49.1:-47.4	278	8:10	3305 to bottom	8.8 ± 1.5	0.07 ± 0.01	0.00 ± 0.01	2.04	34.908
Deep Labrador Current 53°N										
1990-99	7:15	-53.9:-50.9	364	8:11	2615 to bottom	-5.2 ± 0.9	-0.04 ± 0.01	0.00 ± 0.01	1.92	34.900
2000-09	10:14	-53.8:-53.1	89	7:10	1956 to bottom	-8.4 ± 3.9	-0.07 ± 0.05	0.00 ± 0.01	2.24	34.893
2010-19	14:25	-51.5:-49.2	424	7:10	2314 to bottom	-11.4 ± 6.8	-0.11 ± 0.09	0.06 ± 0.03	2.37	34.911
Deep Western Boundary Current 47°N										
1990-99	7:14	-48.0:-44.4	310	7:10	2859 to bottom	-30.1 ± 10.4	-0.31 ± 0.13	0.00 ± 0.01	2.64	34.922
2000-09	7:14	-42.9:-39.5	257	7:10	2820 to bottom	-37.5 ± 5.7	-0.34 ± 0.07	-0.01 ± 0.01	2.30	34.909
Deep Western Boundary Current 36°N										
2000-09	1:13	-71.7:-67.3	406	7:9	2682 to bottom	-34.5 ± 8.7	-0.29 ± 0.10	0.01 ± 0.01	2.13	34.906
Deep Western Boundary Current 24.5°N										
1990-99	16:32	-72.6:-62.7	1002	7:10	2553 to 5630	-23.8 ± 10.8	-0.27 ± 0.11	0.01 ± 0.02	2.88	34.954
2000-09	34:46	-72.0:-56.9	556	7:10	2572 to 5534	-18.3 ± 9.8	-0.22 ± 0.10	0.02 ± 0.01	3.10	34.963
2010-19	46:76	-70.7:-54.6	1624	7:10	2507 to 5741	-30.4 ± 7.3	-0.33 ± 0.07	0.01 ± 0.01	2.72	34.941

Deep Western Boundary Current 11°S										
1990-99	1:8	-35.7:-35.1	88	6:8	1323 to 2561	-17.3 ± 2.2	-0.23 ± 0.03	0.02 ± 0.01	3.39	34.902
Deep Western Boundary Current 19°S										
1990-99	1:7	-37.4:-35.8	168	6:9	1493 to 3370	-20.8 ± 7.2	-0.25 ± 0.09	0.00 ± 0.02	2.98	34.927
Deep Western Boundary Current 24°S										
2000-09	1:20	-41.0:-33.1	808	6:9	1375 to 2946	-29.0 ± 9.0	-0.33 ± 0.10	0.02 ± 0.01	2.92	34.891
2010-19	1:25	-41.0:-31.5	967	6:9	1403 to 3145	-27.5 ± 7.1	-0.32 ± 0.08	-0.02 ± 0.01	2.91	34.899
Deep Western Boundary Current 30°S										
1990-99	1:15	-47.2:-42.9	443	6:9	1336 to 2177	-26.6 ± 5.1	-0.32 ± 0.06	0.02 ± 0.01	3.06	34.820
2000-09	6:14	-46.3:-43.6	282	6:9	1674 to 2861	-25.9 ± 5.0	-0.32 ± 0.06	-0.01 ± 0.02	3.11	34.830
2010-19	1:23	-47.7:-39.5	833	6:9	1368 to 2580	-27.9 ± 1.9	-0.32 ± 0.02	0.01 ± 0.01	2.93	34.840
Deep Western Boundary Current 45°S										
1990-99	7:12	-57.8:-55.8	162	5:9	717 to 3352	-49.1 ± 7.0	-0.53 ± 0.07	-0.20 ± 0.04	2.73	34.441
Deep Eastern Boundary Current 24°S										
2000-09	45:52	-15.0:11.7	348	6:9	1416 to 4141	-13.7 ± 5.5	-0.14 ± 0.05	0.00 ± 0.01	2.59	34.829
2010-19	74:85	-4.1:0.4	457	6:9	1438 to 5089	-9.7 ± 6.1	-0.12 ± 0.06	-0.01 ± 0.01	3.03	34.786
Deep Eastern Boundary Current 30°S										
1990-99	83:100	0.6:11.8	1086	7:9	2502 to 3833	-8.3 ± 4.6	-0.08 ± 0.05	0.00 ± 0.01	2.48	34.828
2000-09	85:99	1.1:10.0	852	7:9	2494 to 3781	-9.7 ± 3.5	-0.09 ± 0.03	0.00 ± 0.01	2.44	34.833
2010-19	97:114	3.3:12.5	887	7:9	2544 to 3932	-8.6 ± 3.4	-0.08 ± 0.03	0.01 ± 0.01	2.31	34.852
Deep Eastern Boundary Current 45°S										
1990-99	80:87	10.9:14.6	415	7:9	2358 to 3153	-6.4 ± 6.3	-0.06 ± 0.06	0.01 ± 0.01	2.22	34.860

315

320

Table 4: Characteristics of each abyssal-layer current found at every section.

Decade	Stations	Long (°E)	Dist (km)	Layers	Depth (m)	Mass Trans (Sv)	Heat Trans (PW)	Fw Total (Sv)	TWT (°C)	TWS
Antarctic Bottom Water – West MAR 45°S										
1990-99	8:50	-57.4:-17.4	3144	10:11	3838 to bottom	4.7 ± 1.5	0.01 ± 0.01	0.00 ± 0.01	0.41	34.697
Antarctic Bottom Water – East MAR 45°S										
1990-99	54:83	-12.0:12.4	2505	10:11	4560 to bottom	-0.9 ± 1.6	0.01 ± 0.01	0.00 ± 0.01	1.18	34.777
Antarctic Bottom Water – West MAR 30°S										
1990-99	9:59	-45.7:-17.7	2725	10:11	3549 to bottom	3.9 ± 1.3	0.01 ± 0.01	0.00 ± 0.01	0.46	34.722
2000-09	9:58	-45.7:-19.0	2599	10:11	3510 to bottom	3.3 ± 1.3	0.01 ± 0.01	0.00 ± 0.01	0.74	34.750
2010-19	9:61	-45.4:-18.2	2639	10:11	3683 to bottom	3.5 ± 1.5	0.01 ± 0.01	0.00 ± 0.01	0.53	34.730
Antarctic Bottom Water – East MAR 30°S										
1990-99	86:99	2.3:11.0	842	10:11	4630 to bottom	-0.3 ± 1.0	0.00 ± 0.01	0.00 ± 0.01	0.98	34.760
2000-09	88:100	2.8:11.0	788	10:11	4761 to bottom	0.1 ± 1.0	0.00 ± 0.01	0.00 ± 0.01	-1.12	34.561
2010-19	96:113	2.8:11.9	877	10:11	4723 to bottom	0.5 ± 0.9	0.00 ± 0.01	0.00 ± 0.01	0.66	34.729
Antarctic Bottom Water – West MAR 24°S										
2000-09	11:43	-38.0:-17.0	2138	10:11	4552 to bottom	0.5 ± 2.3	0.00 ± 0.01	0.00 ± 0.01	-0.87	34.568
2010-19	11:54	-38.0:-14.8	2362	10:11	4568 to bottom	1.9 ± 2.0	0.01 ± 0.01	0.00 ± 0.01	0.17	34.691
Antarctic Bottom Water – East MAR 24°S										
2000-09	79:85	7.2:10.5	331	10:11	4089 to bottom	1.0 ± 2.0	0.00 ± 0.01	0.00 ± 0.01	0.97	34.756
2010-19	99:106	7.2:9.7	253	10:11	4273 to bottom	0.3 ± 1.4	0.00 ± 0.01	0.00 ± 0.01	0.91	34.752
Antarctic Bottom Water – West MAR 19°S										
1990-99	1:31	-37.4:-19.2	1914	10:11	4259 to bottom	1.9 ± 1.4	0.00 ± 0.01	-0.02 ± 0.01	0.08	34.683
Antarctic Bottom Water – West MAR 11°S										
1990-99	6:42	-35.2:-17.0	1989	10:11	4377 to bottom	1.2 ± 1.2	0.00 ± 0.01	0.00 ± 0.01	0.08	34.682
Antarctic Bottom Water – West MAR 24.5°N										
1990-99	11:44	-75.5:-54.7	2103	10:11	5608 to bottom	0.1 ± 0.9	0.01 ± 0.01	0.00 ± 0.01	0.61	34.811
2000-09	11:64	-76.8:-53.7	2322	10:11	5198 to bottom	0.7 ± 0.9	0.00 ± 0.01	0.00 ± 0.01	1.49	34.848
2010-19	19:80	-76.9:-52.3	2474	10:11	5310 to bottom	0.3 ± 1.3	0.01 ± 0.01	0.00 ± 0.01	5.47	35.304

.325